



ALMA DEEP FIELD IN SSA22: SOURCE CATALOG AND NUMBER COUNTS

HIDEKI UMEHATA^{1,2,3}, YOICHI TAMURA², KOTARO KOHNO^{2,4}, R. J. IVISON^{3,5}, IAN SMAIL⁶, BUNYO HATSUKADE⁷,
 KOUICHIRO NAKANISHI^{7,8}, YUTA KATO^{7,9}, SOH IKARASHI¹⁰, YUICHI MATSUDA^{7,8}, SEIJI FUJIMOTO¹¹, DAISUKE IONO^{7,8},
 MINJU LEE^{7,9}, CHARLES C. STEIDEL¹², TOMOKI SAITO¹⁴, D. M. ALEXANDER⁶, MIN S. YUN¹³, AND MARIKO KUBO^{7,11}

¹The Open University of Japan, 2-11 Wakaba, Mihama-ku, Chiba 261-8586, Japan; hideki.umehata@ouj.ac.jp

²Institute of Astronomy, School of Science, The University of Tokyo, 2-21-1 Osawa, Mitaka, Tokyo 181-0015, Japan

³European Southern Observatory, Karl-Schwarzschild-Str. 2, D-85748 Garching, Germany

⁴Research Center for the Early universe, The University of Tokyo, 7-3-1 Hongo, Bunkyo, Tokyo 113-0033, Japan

⁵Institute for Astronomy, University of Edinburgh, Royal Observatory, Blackford Hill, Edinburgh EH9 3HJ, UK

⁶Centre for Extragalactic Astronomy, Department of Physics, Durham University, South Road, Durham, DH1 3LE, UK

⁷National Astronomical Observatory of Japan, 2-21-1 Osawa, Mitaka, Tokyo 181-8588, Japan

⁸Department of Astronomy, School of Science, SOKENDAI (The Graduate University for Advanced Studies), Osawa, Mitaka, Tokyo 181-8588, Japan

⁹Department of Astronomy, Graduate school of Science, The University of Tokyo, 7-3-1 Hongo, Bunkyo-ku, Tokyo 133-0033, Japan

¹⁰Kapteyn Astronomical Institute, University of Groningen, P.O. Box 800, 9700AV Groningen, The Netherlands

¹¹Institute for Cosmic Ray Research, The University of Tokyo, Kashiwa, Chiba 277-8582, Japan

¹²California Institute of Technology, MS 249-17, Pasadena, CA 91125, USA

¹³Department of Astronomy, University of Massachusetts, Amherst, MA 01003, USA

¹⁴Nishi-Harima Astronomical Observatory, Centre for Astronomy, University of Hyogo, 407-2 Nichigaichi, Sayo-cho, Sayo, Hyogo 679-5313, Japan

Received 2016 July 15; revised 2016 November 21; accepted 2016 November 28; published 2017 January 20

ABSTRACT

We present results from a deep $2' \times 3'$ (comoving scale of $3.7 \text{ Mpc} \times 5.5 \text{ Mpc}$ at $z = 3$) survey at 1.1 mm, taken with the Atacama Large Millimeter/submillimeter Array (ALMA) in the SSA22 field. We observe the core region of a $z = 3.09$ protocluster, achieving a typical rms sensitivity of $60 \mu\text{Jy beam}^{-1}$ at a spatial resolution of $0''.7$. We detect 18 robust ALMA sources at a signal-to-noise ratio (S/N) > 5 . Comparison between the ALMA map and a 1.1 mm map, taken with the AzTEC camera on the Atacama Submillimeter Telescope Experiment (ASTE), indicates that three submillimeter sources discovered by the AzTEC/ASTE survey are resolved into eight individual submillimeter galaxies (SMGs) by ALMA. At least 10 of our 18 ALMA SMGs have spectroscopic redshifts of $z \simeq 3.09$, placing them in the protocluster. This shows that a number of dusty starburst galaxies are forming simultaneously in the core of the protocluster. The nine brightest ALMA SMGs with S/N > 10 have a median intrinsic angular size of $0''.32_{-0.06}^{+0.13}$ ($2.4_{-0.4}^{+1.0}$ physical kpc at $z = 3.09$), which is consistent with previous size measurements of SMGs in other fields. As expected, the source counts show a possible excess compared to the counts in the general fields at $S_{1.1\text{mm}} \geq 1.0 \text{ mJy}$, due to the protocluster. Our contiguous mm mapping highlights the importance of large-scale structures on the formation of dusty starburst galaxies.

Key words: catalogs – galaxies: high-redshift – galaxies: star formation – galaxies: starburst – galaxies: structure

1. INTRODUCTION

The history of galaxy formation and evolution appears to be linked to the growth of cosmic large-scale structure. In the present-day universe, clusters of galaxies represent some of the densest environments. Massive and passive elliptical galaxies preferentially reside in cluster cores (e.g., Dressler 1980; Postman & Geller 1984). Recent works have suggested that the brightest cluster galaxies at the center of clusters at $z = 1$ – 2 are relatively evolved, and hence they experienced rapid growth at earlier epochs (e.g., Collins et al. 2009; Gobat et al. 2011). Galaxy cluster archaeology and cosmological simulations suggest the rapid growth of massive ellipticals in high-density regions at $z \gtrsim 2$ – 3 (e.g., Nelan et al. 2005; De Lucia et al. 2006). Therefore, uncovering intense star-forming activity in protoclusters at such high redshifts is of great importance for understanding galaxy and cluster formation in the era when they actively assembled their stars. Such actively star-forming galaxies are expected to be enshrouded by dust, which renders them difficult to observe at rest-frame UV to optical wavelengths. Their spectral energy distributions (SEDs) thus should be dominated by far-infrared (FIR) emission, and therefore observing at FIR to submm/mm wavelengths may be essential

to uncover these dusty galaxies (so-called submillimeter galaxies or SMGs; for reviews, see Blain et al. 2002; Casey et al. 2014).

Extensive efforts have been made to search for and identify such obscured star-forming galaxies in protoclusters at $z > 2$, using submm/mm bolometer cameras onboard single-dish telescopes, such as AzTEC (e.g., Tamura et al. 2009; Capak et al. 2011; Umehata et al. 2014), SCUBA (e.g., Blain et al. 2004; Daddi et al. 2009), SCUBA2 (e.g., Casey et al. 2015), and LABOCA (e.g., Dannerbauer et al. 2014; Clements et al. 2016) as well as FIR to submm/mm satellites, including *Herschel* (e.g., Kato et al. 2016) and *Planck* (e.g., Planck Collaboration et al. 2015). Although these single-dish telescopes are beneficial to cover wide area and find bright SMGs, their relatively poor angular resolution (FWHM $\gtrsim 15''$ – $30''$) and sensitivity limits (due to source confusion) have prevented us from obtaining accurate identifications for sources and/or revealing less-extreme dusty galaxies. The advent of the Atacama Large Millimeter/submillimeter Array (ALMA) allows us to break through these limitations. Contiguous ALMA mosaic imaging is able to open a window for submm/mm deep surveys with sub-arcsec resolution (e.g., Tadaki

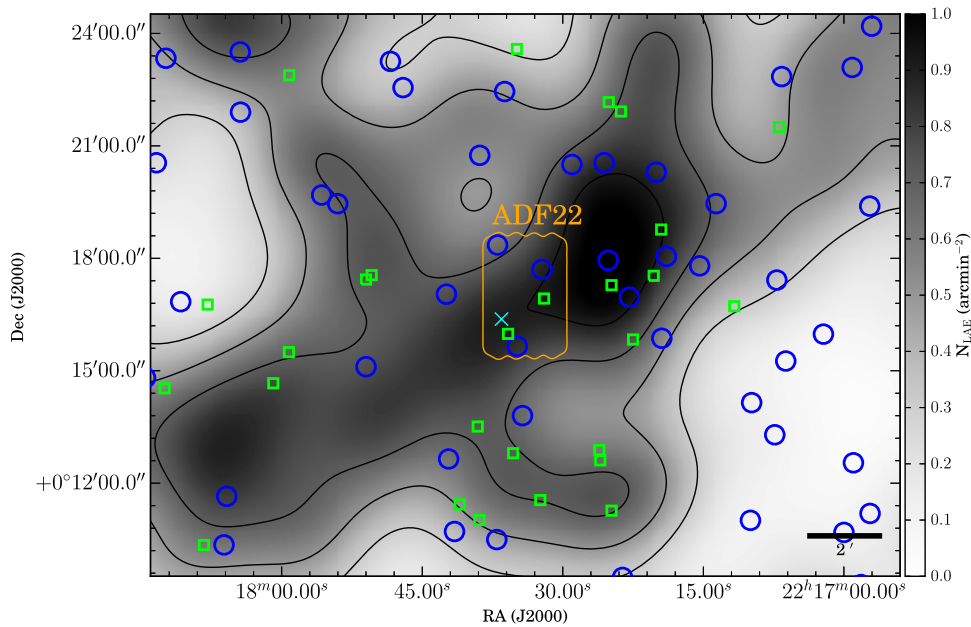


Figure 1. The location of the observed area (named ADF22) on the $z = 3.09$ LAE candidate density map (Hayashino et al. 2004). The orange line shows the area we mapped with ALMA to a limit corresponding to 50% sensitivity of the final mosaic map (same as Figure 3). The gray scales show the surface number density of LAE candidates at $z \sim 3.09$, and the contours represent the smoothed LAE density of 0.3, 0.5, 0.7, and 0.9 in units of arcmin^{-2} , which outlines the $z = 3.1$ protocluster (Hayashino et al. 2004). The blue circles show the 1.1 mm sources discovered by the AzTEC/ASTE survey ($\geq 3.5\sigma$; Umehata et al. 2014). Their diameters are 30 arcsec, which is equivalent to the angular resolution of the AzTEC map. The green squares show the $z \sim 3.09$ LAB positions (Matsuda et al. 2004) and the cyan cross indicates a $z = 3.09$ QSO (Steidel et al. 1998). ADF22 is located near the LAE density peak and contains three submm sources, two bright LABs, and one QSO.

et al. 2015; Aravena et al. 2016; Dunlop et al. 2016; Hatsukade et al. 2016; Walter et al. 2016).¹⁵

We utilized ALMA to conduct a deep imaging survey toward a well-studied protocluster at $z = 3.09$ in the SSA22 field. The protocluster was originally discovered as a redshift spike of Lyman-break galaxies (LBGs) and Ly α emitters (LAEs) by Steidel et al. (1998), Steidel et al. (2000) and was proposed as an ancestor of present-day clusters such as Coma. A remarkable LAE density peak (~ 6 times the average surface density) spreading over tens of comoving Mpc has been found among a huge filamentary structure (>100 comoving Mpc) traced by LAEs (Steidel et al. 2000; Hayashino et al. 2004; Matsuda et al. 2005; Yamada et al. 2012). Distant red galaxies (DRGs) and K -band selected galaxies are found to be more abundant in the core of the protocluster than the field, which supports the elevated formation of massive galaxies there (Uchimoto et al. 2012; Kubo et al. 2013, 2015). In the SSA22 field, a number of submm/mm surveys have been conducted (e.g., Geach et al. 2005, 2014; Scott et al. 2006; Tamura et al. 2009; Umehata et al. 2014). Tamura et al. (2009) discovered a statistical correlation between 15 bright 1.1 mm sources detected by AzTEC and $z \sim 3.09$ LAEs, and suggested that SMGs preferentially formed within the cosmic structure. Umehata et al. (2014) performed counterpart identification of AzTEC sources using radio and near-to-mid infrared data and derived optical to near-infrared photometric redshifts (z_{phot}),

¹⁵ In order to distinguish the submm/mm sources discovered by single-dish telescopes and the galaxies individually observed by interferometers clearly, we utilize the abbreviation SMGs, to indicate the latter—the galaxies individually identified at submm/mm wavelengths—in this paper. We consider all sources discovered by our ALMA survey to be SMGs. As we will show, the individual ALMA SMGs have infrared luminosities comparable with ULIRGs for most cases. The sources discovered by single-dish surveys are simply called “sources” (e.g., AzTEC sources).

which supported the trend found in Tamura et al. (2009) and led to the conclusion that a significant fraction of the AzTEC sources are concentrated in the center of the protocluster.

On the basis of our ALMA survey, in Umehata et al. (2015) we reported the discovery of a concentration of dusty starbursts and X-ray AGNs at the center of a protocluster, and suggested that the large-scale environment plays a key role in the formation of these rare and active populations (see also Alexander et al. 2016). Here, we present the full catalog of the ALMA SMGs and the comprehensive results in terms of mm properties unveiled by ALMA. Our survey design and observations are described in Section 2. We present the procedures for source extraction and catalog selection in Section 3. We compare the ALMA survey with the previous AzTEC survey and derive properties of the sources, including source counts, in Section 4. We conclude with a summary in Section 5. We will report the result of a line search in our survey in N. Hayatsu et al. (2016, in preparation). Throughout the paper, we adopt a cosmology with $\Omega_m = 0.3$, $\Omega_\Lambda = 0.7$, and $H_0 = 70 \text{ km s}^{-1} \text{ Mpc}^{-1}$.

2. THE ALMA DATA

2.1. Field Selection

We observed a $2' \times 3'$ rectangular field and peripheral regions centered at $\alpha = 22^{\text{h}}17^{\text{m}}34^{\text{s}}.0$, $\delta = +00^{\circ}17'00''$ (J2000) at 1.1 mm, using ALMA Band 6 in cycle 2 (Program ID. 2013.1.00162.S, PI. H. Umehata). Hereafter, we name this field “ADF22,” which is an acronym of “ALMA deep field in the SSA22 field.” ADF22 is located at the very center of the cosmic large-scale structure (or “Cosmic Web”) at $z \sim 3$. As illustrated in Figure 1, this area is close to the projected density peak of $z = 3.09$ LAE candidates selected by Subaru/Suprimecam observations with a narrow-band filter (NB497)

Table 1
Summary of ADF22 Observations

SB ^a	Date	Antennas ^b	Baseline ^c	Fields ^d	Synthesized beam ^e	Flux calibrator
SB1	2014 Jun 06	36	20 m–650 m	1–80	0''.59 × 0''.46 (−37.5 deg)	J2148+069
SB2	2014 Jun 07	34	20 m–646 m	1–40	0''.50 × 0''.45 (+18.6 deg)	J2148+069
SB3	2014 Jun 07	34	20 m–646 m	1–80	0''.56 × 0''.47 (−59.6 deg)	J2148+069
SB4	2014 Jun 09	34	20 m–646 m	1–80	0''.61 × 0''.46 (+63.7 deg)	J2148+069
SB5	2014 Jun 10	34	20 m–646 m	1–80	0''.57 × 0''.48 (−64.9 deg)	J2148+069
SB6	2015 Apr 04	33	15 m–328 m	1–103	1''.18 × 0''.87 (−88.6 deg)	Neptune
SB7	2015 Apr 04	33	15 m–328 m	1–103	1''.39 × 0''.81 (−70.1 deg)	Neptune
SB8	2015 Apr 05	35	15 m–328 m	1–103	1''.30 × 0''.90 (−72.3 deg)	Uranus
SB9	2015 Apr 13	40	15 m–349 m	1–103	1''.67 × 1''.11 (+73.9 deg)	Neptune

Notes.

^a Scheduling block.

^b Number of utilized 12 m antennas.

^c Minimum and maximum baseline.

^d Field ID of each pointing (see Figure 2).

^e Synthesized beam size of the map in the case of natural weighting.

(Hayashino et al. 2004). Previous works have unveiled not only the projected density distribution, but also the density structure in three-dimensions (Matsuda et al. 2005). When we only focus on spectroscopically confirmed $z = 3.09$ LAEs and draw a three-dimensional map, ADF22 coincides with the junction of a comoving 50 Mpc-scale filamentary structure (Umehata et al. 2015). This means that ADF22 covers a node of the cosmic large-scale structure, and provides a unique opportunity to examine galaxy formation in such a dense field at this early epoch.

Another important feature is that ADF22 contains a significant number of the most active populations of galaxies that are suggested to preferentially reside in dense environments, including SMGs, QSOs, and Ly α blobs (LABs). There are three 1.1 mm sources discovered by the AzTEC/ASTE survey (Tamura et al. 2009; Umehata et al. 2014). Prior to the present work, one of the three sources, SSA22-AzTEC77 (or SMM J221735+001537), had been proposed as a secure member of the $z = 3.09$ structure (Chapman et al. 2005; Greve et al. 2005; Bothwell et al. 2013), and the other two sources had been also suggested to be at $z \sim 3.09$ (Tamura et al. 2010; Uchimoto et al. 2012; Umehata et al. 2014). One QSO at $z = 3.09$ discovered by Steidel et al. (1998) and two $z \sim 3.09$ LABs listed in Matsuda et al. (2004) are also located within ADF22 (see also Figure 1). ADF22 is thus an excellent region for probing dusty star formation activity in a wide variety of galaxies at the core of the protocluster.

2.2. Observations

We chose the central observing frequency of 263 GHz (1.14 mm), which is similar to that of our previous AzTEC/ASTE survey, 270 GHz, and allows direct comparison with the flux densities of sources from our AzTEC/ASTE and ALMA surveys. Because the size of primary beam of band 6 is larger than that of band 7, this frequency setup is also beneficial to reduce the number of pointings compared to higher frequency. In order to cover a $2' \times 3'$ rectangular field contiguously, we utilized a 103-field mosaic. The spacing between adjacent pointings was 0.72 times the primary beam (FWHM $23''$ at 263 GHz), which was a compromise between the homogeneity of sensitivity and the observing time required to cover as wide an area as possible.

Observations were divided into two campaigns (2014 and 2015 runs), as summarized in Table 1. The first run was conducted on 2014 June 6–10 with 33–36 available 12 m antennas in the C34–4 configuration (longest baseline 650 m) and very good 1.1 mm weather conditions (precipitable water vapor (PWV) of 0.30–1.27 mm). The second run was done on 2015 April 4, 5, and 13 with 32–40 12 m antennas in C32–2 (longest baseline 349 m) and good conditions (PWV of 0.9–1.9 mm). The exposure time per pointing was 30 s for each scheduling block (SB). These observations resulted in an initial on-source time of 2–4.5 minutes per pointing (depending on the individual pointing) and a total on-source time of 386 minutes. We utilized the Time Division Modes correlator, with 4×128 dual polarization channels over the full 8 GHz bandwidth, giving an effective bandwidth of 7.5 GHz after flagging edge channels. The correlator was set up to target two spectral windows of 1.875 GHz bandwidth each, at 15.6 MHz ($\sim 20 \text{ km s}^{-1}$) channel spacing in each sideband. The central frequencies of the four spectral windows are 254.0, 256.0, 270.0, and 272.0 GHz. We note that this frequency range enables us to search for the $^{12}\text{CO}(9-8)$ line ($\nu_{\text{rest}} = 1036.912$ GHz) at $z \sim 3.09$ (we actually found one CO(9–8) emitter, as we describe below. Details will be presented in N. Hayatsu et al. 2016, in preparation.).

The quasar J2148+0657, with flux 1.2 Jy, was observed regularly for amplitude and phase calibration. The absolute flux scale was set using J2148+0657 (for the 2014 run) and Uranus and Neptune (for the 2015 run). We estimate that the absolute flux accuracy is within 20%. This uncertainty in the absolute flux calibration is not included in the following analyses and discussions.

2.3. Data Reduction and Imaging

Data reduction was performed using the Common Astronomy Software Application (CASA; McMullin et al. 2007).¹⁶ The calibration and imaging was performed using CASA version 4.2.2 of the ALMA pipeline and CASA version 4.5.0, respectively. Our analysis is complicated by the fact that our observations were carried out with multiple array configurations. Our observations are composed of nine SBs, as summarized in Table 1. Because

¹⁶ <http://casa.nrao.edu>

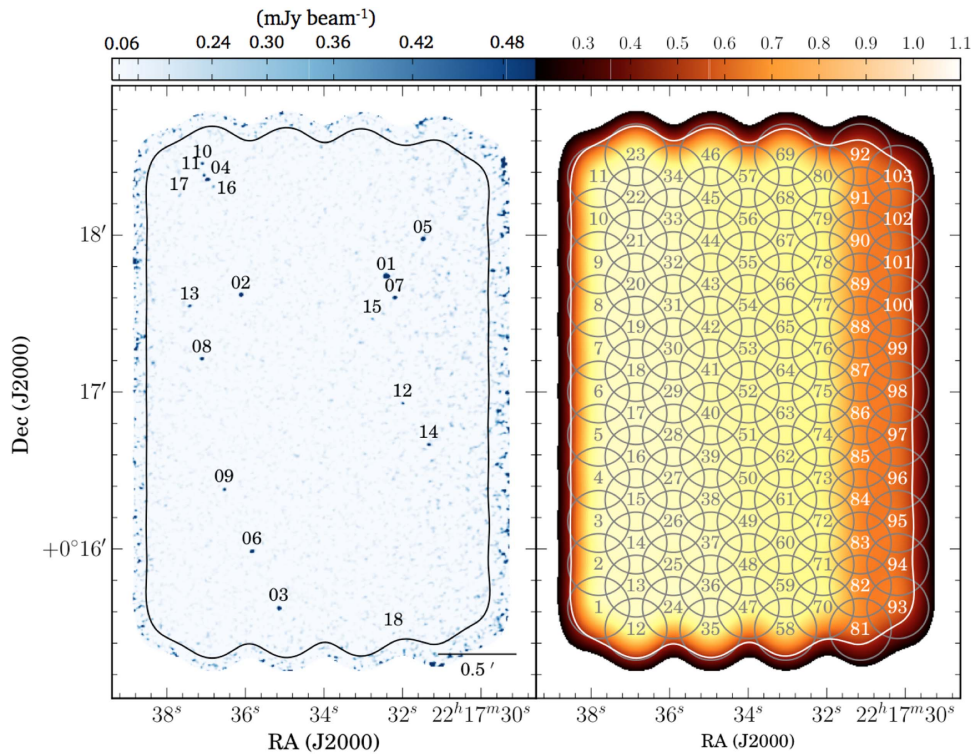


Figure 2. (left) Our ALMA 1.1 mm “FULL/LORES” map of ADF22, corrected for primary beam response. The solid black contour shows the border at which the flux attenuation is 50%. Source extraction was conducted within the 50% coverage area. We also mark the 5σ source positions with identifications (IDs). (right) The “flux” map of ADF22 created by CASA, which shows the response function of flux attenuation within the area. White contours show the 50% attenuation, as in the left figure. Because the ADF22 consists of observations from 103 discrete fields, we denote them as shown in the figure (fields 1–103). The “DEEP/HIRES” map is also created using only 80 pointings (fields 1–80; see Section 2.3). Each circle shows an individual field of view, corresponding to a single pointing ($d = 23''$). For both maps, the outer contour shows the 20% coverage area.

each SB has a different antenna setup, the resulting synthesized beam sizes differ among SBs. There are broadly two array configurations; the maximum baseline lengths of SB6–SB9 (taken in 2015) are systematically shorter than SB1–SB5 (taken in 2014). Because of the difference in the observed area in 2014 and 2015, the western edge fields (fields 81–103 in the right panel of Figure 2) lack longer baseline data and have lower sensitivity (Table 1).

Considering this situation, we first created a $1''$ -tapered map for the entire field (i.e., fields 1–103), which enables us to achieve nearly uniform angular resolution across the map. This larger synthesized beam is more sensitive to extended sources, but suffers from an increased noise level. As we show in the maps of individual sources (Figure 6) and measured sizes of bright sources (Table 3), the resulting angular resolution, $\approx 1''$, seems to be sufficient to detect the majority of sources in this field. We also discuss the possibility that we are missing very extended components in Section 4.1.1.

The uv -data for individual pointings were first combined into a single uv -data set. We then Fourier-transformed the combined data to create a single “dirty” map with natural weighting, by setting the imager mode to “mosaic” and adopting the taper parameter, $\text{outertaper} = 120 k\lambda$. After we measured the rms noise level across the whole dirty map, we repeated the clean process down to 1.5σ , putting a tight clean box ($1'' \times 1''$ in size) around each 5σ source (in a manner similar to that reported by Hodge et al. 2013b). The resulting synthesized beam is $1''.16 \times 1''.02$ in size (P.A. = -80 deg). We denote this map as the FULL/LORES map.

We created another complementary map. Because the five SBs, SB1–SB5, have the longer baseline data with baselines up to $600 k\lambda$, we can achieve a better sensitivity making the best of the longer baselines. For this purpose, we created a second map for 80 pointing field (fields 1–80). We have generally adopted the same procedure described above, but we did not apply any tapering to the map. The second map has a synthesized beam of $0''.70 \times 0''.59$ (P.A. = -80 deg). Hereafter, we call it the DEEP/HIRES map. In the following analyses, we utilize primarily the FULL/LORES map. The DEEP/HIRES map is used for detecting compact faint sources (Section 3) and resolving bright sources (Section 4.2).

The final FULL/LORES map, corrected for the primary beam response, is shown in Figure 2. In the following sections, we consider the effective area; the area in the map within which the primary beam coverage is greater than 50%. This results in a 7.0 arcmin^2 area in the case of the FULL/LORES map (5.8 arcmin^2 for the DEEP/HIRES map). A sensitivity map was constructed utilizing an AIPS task, RMSD, calculating the rms for each $0''.1 \times 0''.1$ pixel using the surrounding 100×100 pixels (or $10''.0 \times 10''.0$) on an image prior to correcting for primary beam response. The correction results in a range of 1σ depth of $52\text{--}170 \mu\text{Jy beam}^{-1}$ with a median value of $75 \mu\text{Jy beam}^{-1}$ (Figure 3) for the FULL/LORES map. In the case of the DEEP/HIRES map, we obtained a range of 1σ depth from $50\text{--}129 \mu\text{Jy beam}^{-1}$ with a median value of $60 \mu\text{Jy beam}^{-1}$ (Figure 3).

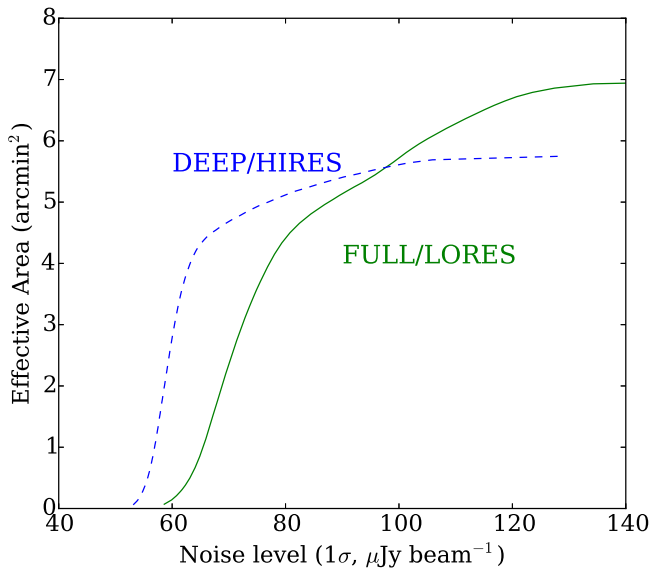


Figure 3. Effective survey area of the FULL/LORES map and the DEEP/HIRES map as a function of 1σ sensitivity. Our survey covers 7.0 arcmin^2 and 5.8 arcmin^2 in total, respectively.

3. THE CATALOG

3.1. Source Extraction and Characterization

Source extraction was performed using the image map and sensitivity map that were not corrected for the primary beam attenuation. First, we utilized the FULL/LORES map. A source-finding algorithm, AEGEAN v1.9.5-56 (Hancock et al. 2012), was used to extract positive sources above 3.5σ . In parallel, we also counted *negative* sources with source-like profiles above 3.5σ during the procedure to estimate the fraction of spurious sources among the detected sources. The cumulative number counts of positive and negative sources as a function of signal-to-noise ratio (S/N) is shown in Figure 4. We found 17 positive sources with $>5\sigma$ and 28 sources with $>4\sigma$. There were no negative sources above 5σ , whereas we found seven negative ones with 4σ – 4.6σ . The results show that the detection limit of 5σ is secure and conservative. Gaussian statistics also support the validity of the threshold. Because the map contains $\approx 32,000$ beams, we would expect less than one spurious peak above 5σ . Therefore, we adopt these 17 sources as secure detections (ADF22.1–ADF22.17; see Table 2).

We also performed the same procedures on the DEEP/HIRES map, independently. As a result, 14 sources were detected at $>5\sigma$, one of which was not detected in the shallower FULL/LORES map. This source (ADF22.18; see Table 2) was added to the catalog of secure detection because there were no negative sources with $>5\sigma$ in the DEEP/HIRES map. Therefore, a total of 18 sources were detected at $S/N > 5$.

In the following analyses and discussion, we mostly focus on the 18 secure sources not affected by spurious features. We show a supplementary catalog of 14 sources detected tentatively in the FULL/LORES and DEEP/HIRES maps, in Appendix A.

The flux densities of the detected sources were measured with the IMFIT task of CASA, using the map after correction for the primary beam attenuation. We adopt the integrated flux density as the flux density of a source, unless it is lower than the peak flux density (e.g., Simpson et al. 2015b). The

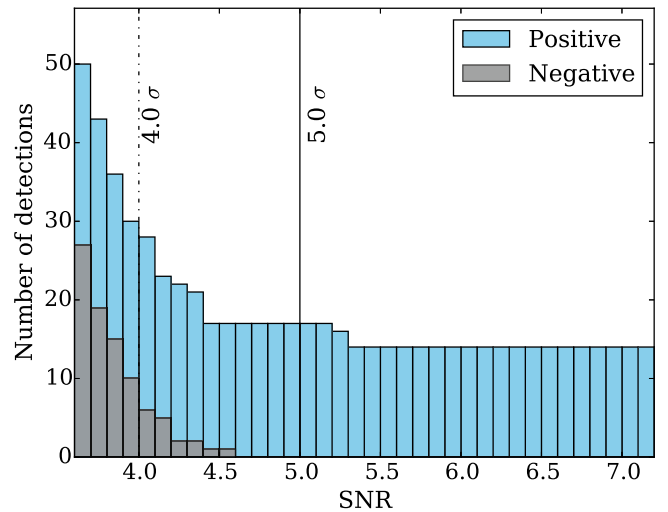


Figure 4. Cumulative number of positive and negative peaks as a function of signal-to-noise ratio (S/N) for the FULL/LORES map. The solid vertical line shows the detection limit (5σ). There are no negative peaks above 5σ , which suggests our adopted detection limit is conservative. The dashed-dotted line shows the threshold for tentative detection.

measurements of fluxes on the two maps are in good agreement with each other. The median ratio of the flux density between the FULL/LORES map and the DEEP/HIRES map is $S^{\text{FULL}}/S^{\text{DEEP}} = 0.96^{+0.00}_{-0.02}$ for the 13 sources detected above 5σ , in both maps.

3.2. Completeness and Flux Boosting

We performed a suite of simulations to evaluate the completeness and boosting effect on our flux measurement. We briefly describe the method below (for more detail, see Hatsukade et al. 2016). Model sources created by scaling the synthesized beam are injected into the image map corrected for primary beam attenuation. The input position is randomly selected to be $>1''.0$ away from $\geq 3\sigma$ sources. We then repeated the same procedures for the source extraction using the artificial map as described in Section 3.1.

The completeness is measured as the recovery rate of the injected model sources; when an input source is detected within $1''.0$ of the injected position with $\geq 4\sigma$, the source is considered to be recovered. Model sources with flux densities over the range $S = 0.02$ – 0.6 mJy in steps of 0.02 mJy are considered and the procedures are repeated 1000 times for each flux density bin ($\Delta S = 0.02 \text{ mJy}$). The results are summarized in Figure 5 as a function of input flux density. The completeness of our source extraction is $\sim 70\%$ at $S/N = 4$ and rises to $\sim 90\%$ at $S/N = 5$. The completeness reaches $\sim 100\%$ at $S/N \gtrsim 6.0$. We consider the completeness in calculating source counts in Section 4.3, although it does not matter significantly for $>5\sigma$ sources.

In the course of the completeness measurement, we also evaluate the effect of flux boosting. It is known that the flux density of sources in a signal-to-noise limited catalog tend to be boosted as a whole due to random noise fluctuations and the shape of the source count distribution (e.g., Hogg & Turner 1998; Scott et al. 2002; Coppin et al. 2006). We plot the ratio of input and output flux density against the input flux density in Figure 5. The results show that the effect is

Table 2
ADF22 Source Properties

(1)	(2)	(3)	(4)	(5)	(6)	(7)	(8)	(9)
ALMA ID	ALMA NAME	ID (U15)	AzTEC ID (mJy)	S_{AzTEC} (J2000)	σ_{ALMA} ($\mu\text{Jy beam}^{-1}$)	$S/N_{\text{ALMA}}^{\text{pk}}$	S_{ALMA} (mJy)	z_{spec}
ADF22.1 ^a	ALMAJ221732.41+001743.8	ADF22a	AzTEC1	$11.3^{+0.9}_{-0.7}$	72	58.1	5.60 ± 0.13	3.092(a)
ADF22.2	ALMAJ221736.11+001736.7	63	31.8	2.02 ± 0.02	...
ADF22.3	ALMAJ221735.15+001537.2	ADF22b	AzTEC77	$2.4^{+0.9}_{-0.8}$	66	27.0	1.89 ± 0.04	3.096(d)
ADF22.4	ALMAJ221736.96+001820.7	...	AzTEC14	$4.5^{+0.8}_{-0.8}$	72	26.6	1.95 ± 0.05	3.091(b)
ADF22.5	ALMAJ221731.48+001758.0	99	20.3	2.43 ± 0.20	...
ADF22.6	ALMAJ221735.83+001559.0	ADF22c	69	19.1	1.45 ± 0.09	3.089(e)
ADF22.7	ALMAJ221732.20+001735.6	ADF22i	AzTEC1	$11.3^{+0.9}_{-0.7}$	86	18.7	1.65 ± 0.07	3.097(c)
ADF22.8	ALMAJ221737.11+001712.3	ADF22d	77	15.0	1.19 ± 0.06	3.090(f)
ADF22.9	ALMAJ221736.54+001622.6	ADF22e	60	12.8	0.82 ± 0.08	3.095(f)
ADF22.10	ALMAJ221737.10+001826.8	...	AzTEC14	$4.5^{+0.8}_{-0.8}$	71	9.8	0.72 ± 0.04	...
ADF22.11	ALMAJ221737.05+001822.3	ADF22f	AzTEC14	$4.5^{+0.8}_{-0.8}$	77	9.5	0.79 ± 0.05	3.093(f)
ADF22.12	ALMAJ221732.00+001655.4	ADF22g	71	8.8	0.63 ± 0.03	3.091(f)
ADF22.13	ALMAJ221737.42+001732.4	81	8.0	0.79 ± 0.05	...
ADF22.14	ALMAJ221731.34+001639.6	99	7.5	0.98 ± 0.13	...
ADF22.15	ALMAJ221732.77+001727.5	79	5.3	0.50 ± 0.08	...
ADF22.16	ALMAJ221736.81+001818.0	ADF22h	AzTEC14	$4.5^{+0.8}_{-0.8}$	77	5.3	0.56 ± 0.07	3.085(f)
ADF22.17	ALMAJ221737.69+001814.4	...	AzTEC14	$4.5^{+0.8}_{-0.8}$	66	5.1	0.60 ± 0.09	...
ADF22.18 ^b	ALMAJ221732.23+001527.8	82	5.3	0.44 ± 0.05	2.105(g)

Notes. (1) ID in this paper. (2) Source name that represents the coordinate in the wcs system. (3) ID defined in Umehata et al. (2015). (4) ID of AzTEC source in Umehata et al. (2014). We list it if an ALMA SMG is located within the $30''$ AzTEC beam. (5) Flux density of AzTEC source (Umehata et al. 2014). (6) 1σ sensitivity at a given source position after the primary beam correction. (7) The signal-to-noise ratio, which is defined as a ratio of peak flux density over the 1σ sensitivity. (8) The flux density and uncertainty measured by the CASA task, IMFIT. (9) Spectroscopic redshift (z_{spec}) if a given source has it. The lines used to determine z_{spec} and references are as follows. (a) $^{12}\text{CO}(3-2)$ (M. Yun et al. 2016, in preparation). (b) $^{12}\text{CO}(9-8)$ (H. Umehata et al. 2016, in preparation; N. Hayatsu et al. 2016, in preparation). (c) $[\text{C II}] 157.7 \mu\text{m}$ (H. Umehata et al. 2016, in preparation). (d) $^{12}\text{CO}(3-2)$ (Bothwell et al. 2013, see also Chapman et al. 2005, Greve et al. 2005). (e) $\text{Ly}\alpha$ (Chapman et al. 2005). (f) $[\text{O III}] \lambda 5007$ (Kubo et al. 2015, 2016). (g) $\text{Ly}\alpha$ (Chapman et al. 2004a).

^a This source was identified as a primary counterpart of SSA22-AzTEC1 using the Submillimeter Array (SMA) in Tamura et al. (2010).

^b The properties of ADF22.18 are measured using the DEEP/HIRES map.

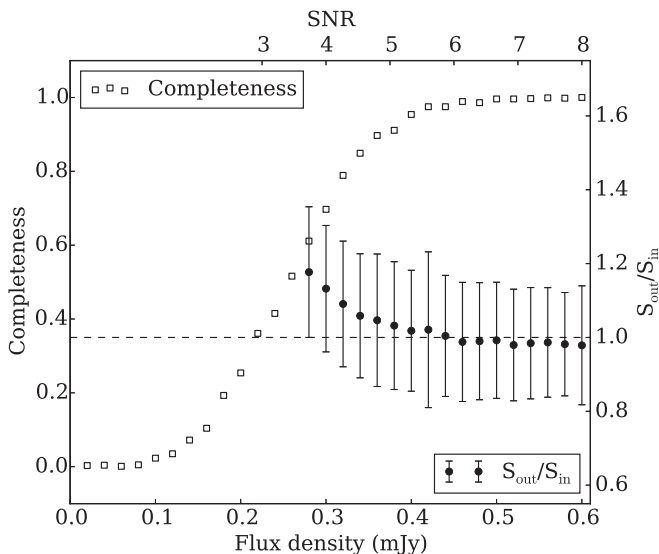


Figure 5. Measured completeness and the ratio between input flux densities of embedded artificial sources and output flux densities for the FULL/LORES map. The lower horizontal axes shows input flux density, corrected for primary beam attenuation. The upper axis shows the corresponding, approximate S/N, calculated assuming the median sensitivity. The 5σ detection limit results in $\geq 90\%$ completeness. We do not consider the flux boosting effect, which is negligible for 5σ sources.

negligible if we consider only those sources detected at $>5\sigma$. Hence we do not consider the flux boosting effect in the following discussion.

3.3. Source Catalog

The measured properties of the ADF22 SMGs are summarized in Table 2. The first column lists the source IDs in this paper, which are generally ranked in terms of S/N. The nine SMGs reported in Umehata et al. (2015) are noted in the second column. There are three AzTEC sources in our field (Umehata et al. 2014). We listed the IDs and flux densities of the corresponding AzTEC source if a given ALMA SMG is located within the AzTEC beam (FWHM; $d = 30''$). We give the flux density, measured by Gaussian fitting with CASA, IMFIT. We note that these measurements are from the FULL/LORES map except for ADF22.18, which was detected at $>5\sigma$ only in the DEEP/HIRES map.

We also report the spectroscopic redshift (z_{spec}), if known. Eleven of the 18 SMGs have z_{spec} , 10 of which have $z \simeq 3.09$. In addition to eight $z \simeq 3.09$ SMGs reported in Umehata et al. (2015), we adopt z_{spec} for three SMGs, ADF22.4, ADF22.7, and ADF22.18. The redshifts of ADF22.4 and ADF22.7 are determined from our recent ALMA observations ($^{12}\text{CO}(9-8)$) at $z = 3.091$ and $[\text{C II}] 157.7 \mu\text{m}$ at $z = 3.097$, respectively; H. Umehata et al. 2016, in preparation). ADF22.18 coincides with a $z = 2.015$ radio source, RG J221732.22+001528.2, reported in Chapman et al. (2004a) with a small projected separation ($0''.4$). We show the ALMA 1.1 mm images of the 18 SMGs in Figure 6.

One reasonable concern regarding the ALMA source catalog is the overlap between the previously known galaxy populations and our newly discovered ALMA SMGs. Within the survey area of the FULL/LORES map (Figure 2), there are 19

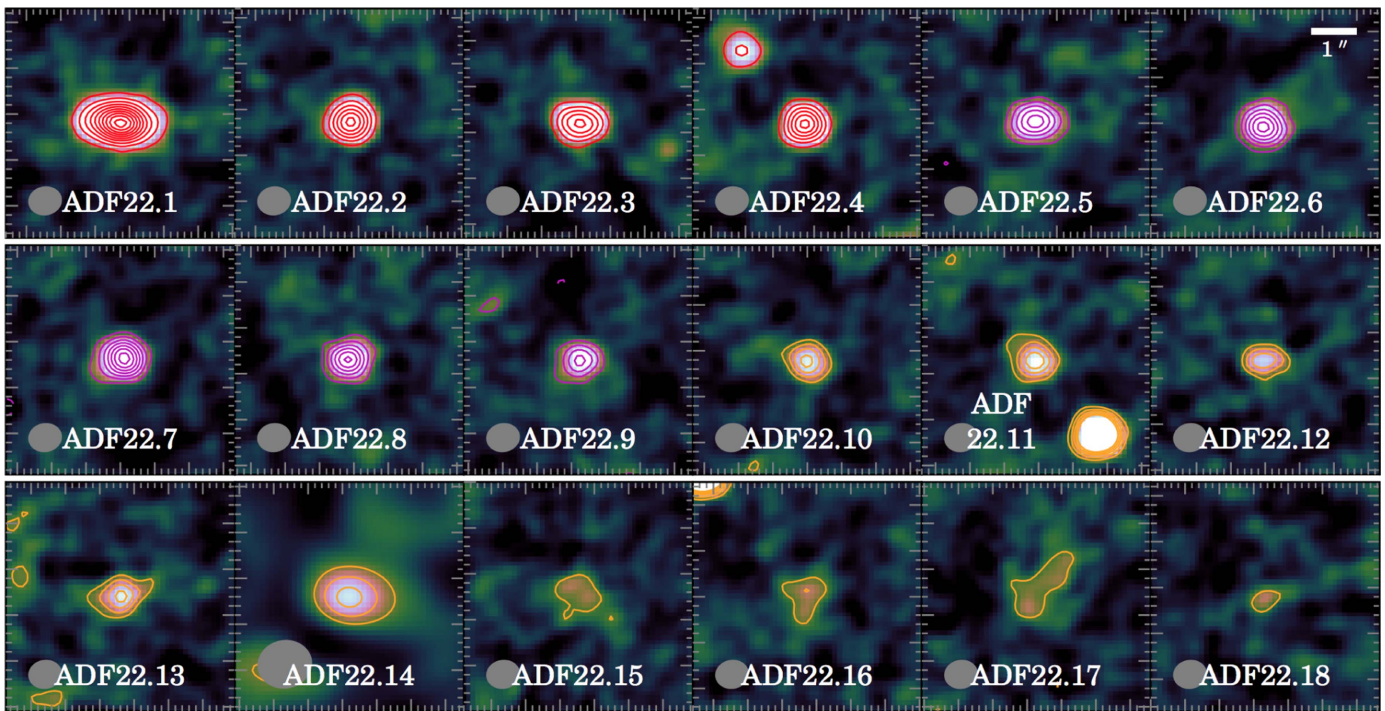


Figure 6. ALMA 1.1 mm continuum maps of 18 sources in ADF22. Each map is $5'' \times 5''$ in size. We show the DEEP/HIRES map to display the better angular resolution image. We use the FULL/LORES map only for ADF22.14, which is not covered by the DEEP/HIRES map (see Figure 2 for the source distributions and covered area of the FULL/LORES and DEEP/HIRES map). IDs are shown in the bottom in the maps, and synthesized beams are displayed in the bottom left of each map. The 1.1 mm ALMA contours are in steps of 5σ starting at $\pm 5\sigma$ (red, ADF22.1–ADF22.4), in steps of 3σ starting at $\pm 3\sigma$ (magenta, ADF22.5–ADF22.9), and in steps of 2σ starting at $\pm 3\sigma$ (orange, ADF22.10–ADF22.18).

LAEs (Matsuda et al. 2005; Nestor et al. 2013; Erb et al. 2014), five LBGs (Steidel et al. 2003; Nestor et al. 2013; Erb et al. 2014), and 10 K-band selected galaxies (Kubo et al. 2015, 2016) within the protocluster (i.e., with $z_{\text{spec}} = 3.06\text{--}3.12$; Hayashino et al. 2004; Matsuda et al. 2005). None of the ALMA SMGs (including candidates in the supplementary source catalog) have LAE/LBG counterparts, which shows that these rest-frame UV selected galaxies are clearly separated populations, compared to galaxies individually detected by ALMA. In contrast, five out of 10 K-band selected galaxies are securely detected by ALMA. Therefore, such a relatively massive galaxy population (stellar mass, $\gtrsim 10^{10\text{--}11} M_{\odot}$; Kubo et al. 2013) selected at rest-frame optical wavelengths appears to significantly overlap with the ALMA population. This trend is broadly consistent with recent works in SXDF (Tadaki et al. 2015) and HUDF (Aravena et al. 2016; Dunlop et al. 2016), as well as previous studies of ALMA SMGs (Simpson et al. 2014). We summarize the relationship to other populations in Appendix B.

4. DISCUSSION

4.1. Resolving the AzTEC Map with ALMA

Several hundred submm/mm sources discovered by single-dish telescopes have been observed by submm/mm interferometers to date. Some appear to resolve into multiple, individual SMGs, whereas others have a unique counterpart above a given detection limit (e.g., Gear et al. 2000; Tacconi et al. 2006; Younger et al. 2008; Wang et al. 2011; Barger et al. 2012; Smolčić et al. 2012a; Hodge et al. 2013a; Miettinen et al. 2015; Simpson et al. 2015a). For instance, Barger et al. (2012) reported that, using the SMA, three of 16 SCUBA

sources are composed of multiple objects. From ALMA observations, Hodge et al. (2013b) and Simpson et al. (2015a) suggested that $\sim 30\text{--}40\%$ of LABOCA or bright SCUBA2 sources (with flux densities of $S_{870\mu\text{m}} = 4\text{--}15$ mJy and $S_{850\mu\text{m}} \sim 8\text{--}16$ mJy, respectively) are resolved into multiple SMGs brighter than $S_{870\mu\text{m}} \sim 1$ mJy, making most of the components “ULIRGs.” These results suggest that the relatively poor angular resolution of single-dish imaging ($\gtrsim 15''$) causes significant source blending and complicates our interpretation of the nature of SMGs. ALMA enables us now to resolve not only individual single-dish sources, but also relatively faint sources spread over a wider area.

4.1.1. Comparison of the AzTEC and ALMA Map

The AzTEC/ASTE survey of SSA22 by Tamura et al. (2009) and Umehata et al. (2014) presented a 1.1 mm image of ADF22. The $30''$ resolution image has a 1σ depth of 0.7 mJy beam^{-1} and detects three sources above a 3.5σ detection threshold within ADF22 (SSA22-AzTEC1, SSA22-AzTEC14, and SSA22-AzTEC77; hereafter AzTEC1, AzTEC14, and AzTEC77, respectively). Two of the three AzTEC sources, AzTEC1 and AzTEC14, have two and five ALMA SMGs located within the FWHM of the AzTEC beam, respectively. In contrast, AzTEC77 has only one associated ALMA SMG (Figure 7).¹⁷ In summary, three AzTEC sources are resolved into eight ALMA SMGs. The result is in line with previous

¹⁷ AzTEC77 shows an elongated profile, which should be caused by ADF22.6, as illustrated in Figure 7. Therefore, the profile itself should reflect the two ALMA SMGs. However, ALMA6 is located at outside of the AzTEC beam of AzTEC77 and so does not contribute significantly to the measured flux of AzTEC77. Hence, here we treat ADF22.3 as an unique counterpart of AzTEC77.

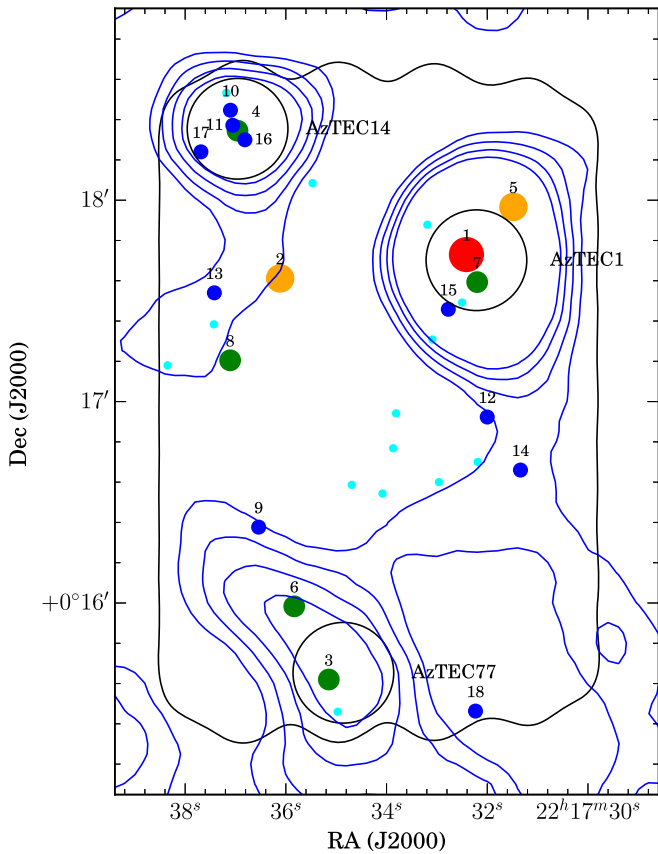


Figure 7. The distributions of the ALMA SMGs and AzTEC sources in the ADF22. Filled circles represent the ALMA SMGs, the size and color of which stand for their flux density (red: $S_{1.1\text{mm}} > 5$ mJy, orange: $2 \text{ mJy} < S_{1.1\text{mm}} \leq 5$ mJy, green: $1 \text{ mJy} < S_{1.1\text{mm}} \leq 2$ mJy, blue: $S_{1.1\text{mm}} \leq 1.0$ mJy). The associated number is the ALMA source ID in this paper. Filled cyan circles represent the positions of ALMA sources in the supplementary catalog. The positions of three AzTEC sources are shown using large black circles, the diameters of which is equivalent to the beam FWHM of the AzTEC map ($d = 30''$). We also plot 0, 1, 2, and 3 σ contours of the AzTEC 1.1 mm map ($1\sigma = 0.7$ mJy; Umehata et al. 2014). The black contour is the 50% coverage area of the FULL/LORES map, which is same as Figure 2. The ALMA mosaic revealed the source distribution below the AzTEC detection limit across the area.

ALMA studies following up single-dish submm/mm sources with interferometers, which reports that a significant fraction of submm/mm sources detected by single-dish telescopes are found to be intrinsically multiple SMGs (e.g., Hodge et al. 2013a).

To check the relative flux scales, we compared the flux density between the AzTEC sources and the associated ALMA SMGs. For the AzTEC sources, deboosted flux densities in Umehata et al. (2014) (S^{AzTEC}) are considered here. Regarding the measurements for the ALMA SMGs, we calculate the sum of the flux densities of the SMGs with $\geq 5\sigma$ within the FWHM of the AzTEC beam (S^{ALMA}). Figure 8 shows the results for the three AzTEC sources. The ratio between the two, $S^{\text{ALMA}}/S^{\text{AzTEC}}$, is in agreement within error bars for AzTEC77 and AzTEC14, which suggests that the ALMA SMGs discovered from this survey account for the majority of the flux density of the AzTEC sources. However, the situation is not the same for AzTEC1, the brightest AzTEC source in the SSA22 field, which has $S^{\text{ALMA}}/S^{\text{AzTEC}} = 0.64 \pm 0.05$. The discrepancy could imply the existence of additional components of 1.1 mm emission not accounted for in the ALMA map. One possibility

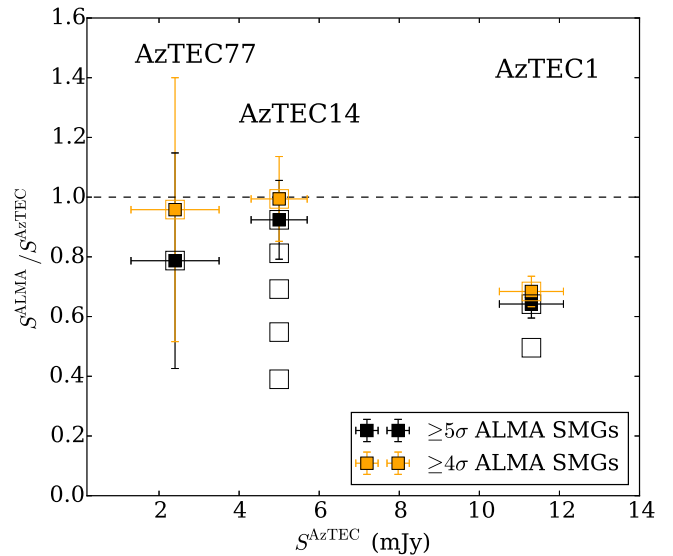


Figure 8. A comparison of the flux measurements in the AzTEC and ALMA maps for the three AzTEC sources; AzTEC1, AzTEC14, and AzTEC77. Here, S^{AzTEC} shows the flux density of the AzTEC sources and S^{ALMA} stands for the integration of that of the ALMA SMGs within the AzTEC beam. The filled black squares show the flux ratio, $S^{\text{ALMA}}/S^{\text{AzTEC}}$, as a function of S^{AzTEC} , considering ALMA SMGs with $\geq 5\sigma$. The filled orange squares show the flux ratio, including the sources in the supplementary catalog. Empty squares represent the ratio in the case of cumulative flux density of individual ALMA SMGs, which are in order of flux density. Although S^{AzTEC} and S^{ALMA} match within the range of error for AzTEC14 and AzTEC77, S^{ALMA} is only $64 \pm 5\%$ of S^{AzTEC} in the case of AzTEC1.

is that we are missing a number of fainter and/or diffuse sources (e.g., Hodge et al. 2013a; Simpson et al. 2015a). If we include sources in the supplementary catalog with $S/N = 4-5$, then the flux ratio $S^{\text{ALMA}}/S^{\text{AzTEC}}$ gets closer to unity for all three AzTEC sources (Figure 8). However, these sources are still insufficient to explain the case of AzTEC1. Much fainter sources might also contribute to the AzTEC sources for AzTEC1.

Tamura et al. (2010) gave us another clue. They reported the $860 \mu\text{m}$ flux density of ADF22.1, $S_{860\mu\text{m}} = 12.2 \pm 2.3$ mJy, using the Submillimeter Array.¹⁸ They obtained the natural-weighted synthesized beam, $3''.43 \times 1''.92$ (P.A. 34.3 deg), and found that the source was likely not to be resolved. If we predict a 1.1 mm flux density of ADF22.1, using an averaged SMG template from the ALESS survey (Swinbank et al. 2014) scaled to the $860 \mu\text{m}$ flux density, the expected value is $S_{1.1\text{mm}} \approx 6.0$ mJy. The estimate is broadly consistent with our measurement, which suggests that we are measuring the vast majority of the dust emission from ADF22.1.

There are two ALMA SMGs, ADF22.5 and ADF22.15, located just outside of the beam for AzTEC1 (Figure 7). If we take into account ADF22.5 and ADF22.15, the integral of the flux densities of the ALMA SMGs approach the flux density of AzTEC1 ($S^{\text{ALMA}}/S^{\text{AzTEC}} = 0.94 \pm 0.07$). In order to investigate whether these SMGs indeed contribute to the flux density of AzTEC1 in the AzTEC map, we made a “model” AzTEC image convolving the ALMA map with a Gaussian kernel with a FWHM of $30''$. AzTEC1 has flux density 7.1 mJy in the model map, which is consistent with the sum of flux density of the ALMA SMGs within the beam for AzTEC1, not including

¹⁸ Tamura et al. (2010) found only one source toward SSA22-AzTEC1, and ADF22.7 was not detected significantly in the paper.

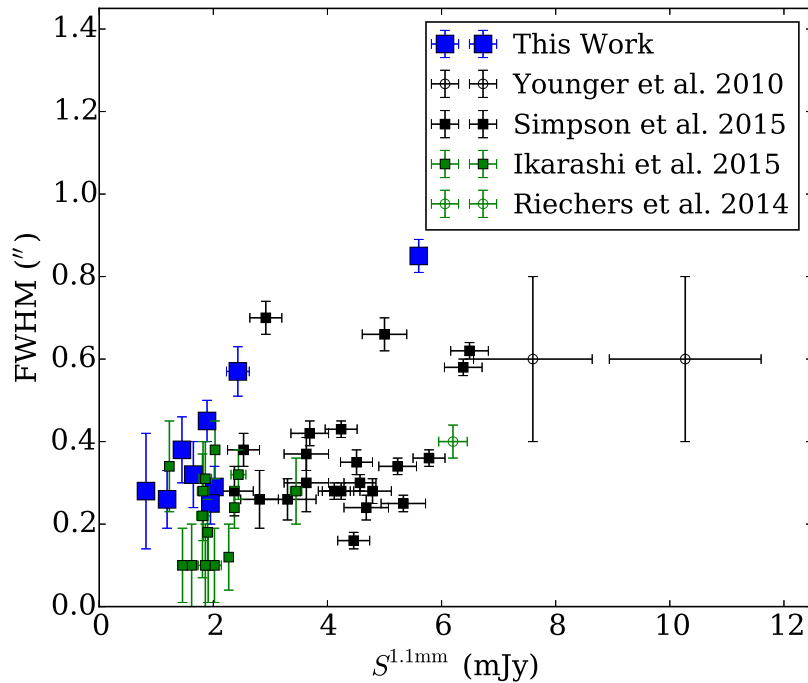


Figure 9. Angular size distribution of the 1.1 mm emission from SMGs as a function of their 1.1 mm flux density. The horizontal axis shows a deconvolved FWHM of the major axis from two-dimensional Gaussian fitting. The results of ADF22 sources are shown. We also show those of previous works (Younger et al. 2010; Riechers et al. 2014; Ikarashi et al. 2015; Simpson et al. 2015b). The flux densities at $870\ \mu\text{m}$ (Simpson et al. 2015b) and at $890\ \mu\text{m}$ (Younger et al. 2010) are scaled to 1.1 mm flux density using $S_{1.1\text{mm}}/S_{870\mu\text{m}} = 0.56$ and $S_{1.1\text{mm}}/S_{890\mu\text{m}} = 0.58$, respectively. We assume a modified black body with typical values for SMGs (spectral index of $\beta = 1.5$, dust temperature of 35 K (e.g., Swinbank et al. 2014), and $z = 2.5$). The source sizes are generally consistent with the works, and there is no clear environmental dependence.

Table 3
Summary of Derived Properties for Nine Sources with $S/N \geq 10$

ALMA ID	Major Axis ($''$)	(kpc)	Minor Axis ($''$)	(kpc)	$L_{8-1000\mu\text{m}}$ ($\log(L_{\odot})$)	SFR_{IR} ($M_{\odot}\ \text{yr}^{-1}$)	Σ_{SFR} ($M_{\odot}\ \text{yr}^{-1}\ \text{kpc}^{-2}$)
ADF22.1	0.85 ± 0.04	6.5 ± 0.3	0.33 ± 0.03	2.5 ± 0.2	$13.0^{+0.2}_{-0.1}$	1100^{+830}_{-210}	40
ADF22.2 ^a	0.29 ± 0.05	2.2 ± 0.4	0.05 ± 0.11	0.4 ± 0.8	$12.6^{+0.2}_{-0.1}$	400^{+300}_{-70}	300
ADF22.3	0.45 ± 0.05	3.4 ± 0.4	0.18 ± 0.08	1.4 ± 0.6	$12.5^{+0.2}_{-0.1}$	370^{+280}_{-70}	50
ADF22.4	0.25 ± 0.05	1.9 ± 0.4	0.04 ± 0.11	0.3 ± 0.8	$12.6^{+0.2}_{-0.1}$	380^{+290}_{-70}	420
ADF22.5 ^a	0.57 ± 0.06	4.4 ± 0.5	0.26 ± 0.06	2.0 ± 0.5	$12.7^{+0.2}_{-0.1}$	480^{+360}_{-90}	30
ADF22.6	0.38 ± 0.08	2.9 ± 0.6	0.30 ± 0.14	2.3 ± 1.1	$12.4^{+0.2}_{-0.1}$	280^{+210}_{-50}	30
ADF22.7	0.32 ± 0.08	2.4 ± 0.6	0.22 ± 0.10	1.7 ± 0.8	$12.5^{+0.2}_{-0.1}$	320^{+240}_{-60}	50
ADF22.8	0.26 ± 0.07	2.0 ± 0.5	0.18 ± 0.05	1.4 ± 0.4	$12.3^{+0.2}_{-0.1}$	230^{+180}_{-40}	50
ADF22.9	0.28 ± 0.14	2.1 ± 1.1	0.26 ± 0.17	2.0 ± 1.3	$12.2^{+0.2}_{-0.1}$	160^{+120}_{-30}	20

Note. Derived properties of the nine sources with $S/N \geq 10$. The second and fourth columns show a deconvolved FWHM of the major and minor axes, derived using IMFIT. The third and fifth columns represent corresponding physical scale. Infrared luminosity ($L_{8-1000\mu\text{m}}$) is estimated using several templates of dusty galaxies as described in Umehata et al. (2015). SFR_{IR} are calculated from $L_{8-1000\mu\text{m}}$, using the empirical calibration by Kennicutt (1998) adjusted for Kroupa initial mass function (Kroupa 2001). We also roughly estimated surface density of SFR (Σ_{SFR}) using SFR_{IR} and derived source size.

^a Because ADF22.2 and ADF22.5 do not have z_{spec} , we assume $z = 3.0$, which is a median redshift of the AzTEC sources (Smolčić et al. 2012b).

ADF22.5 and ADF22.15. Therefore, these two nearby SMGs are likely not to account for the discrepancy. We do not consider a systematic error on the absolute flux accuracy for the AzTEC map throughout the above discussion. Although it is difficult to estimate the influence for our small sample, ALMA surveys of a significant number of AzTEC sources will allow us to examine the effect.

As displayed in Figure 7, we compared the spatial distribution of SMGs discovered by ALMA and the contours of the AzTEC 1.1 mm emission, below the AzTEC detection limit (3.5σ). Our ALMA map has discovered 10 SMGs outside

the AzTEC source positions. We found that nine of the 10 ALMA SMGs are located within or in the vicinity of the area where the 1.1 mm flux density is $0\text{--}2.1\ \text{mJy beam}^{-1}$ in the AzTEC map. This may show that the structure traced by the faint AzTEC emission, below 3σ , reflects the distribution of 1.1 mm sources to a certain degree.

As we reported in Umehata et al. (2014), the AzTEC catalog is significantly incomplete at around 3.5σ (i.e., the detection threshold). The completeness of the AzTEC map is only $\sim 50\%$ at 2 mJy. Among the ADF22 sources with flux density $\sim 2\ \text{mJy}$, two SMGs, ADF22.2 and ADF22.5, are found to be

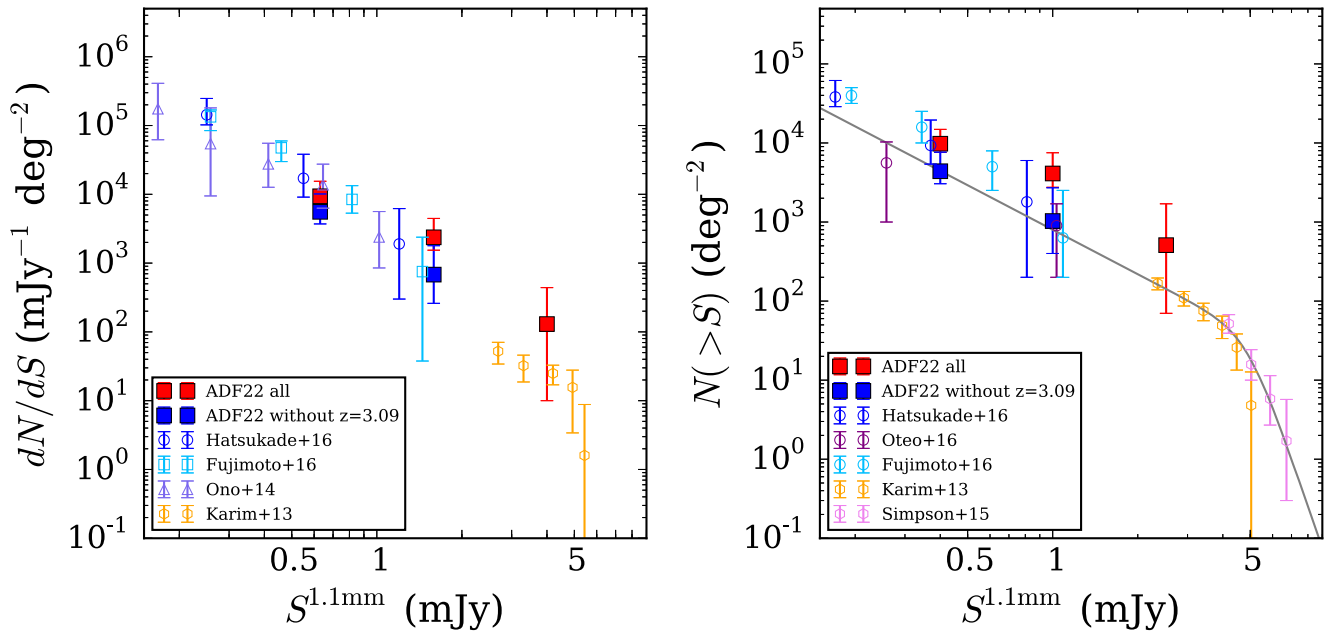


Figure 10. Differential (left panel) and cumulative (right panel) number counts in ADF22 and other fields at 1.1 mm. The counts in ADF22 are calculated in two ways. We show the counts calculated from our full sample of the 17 SMGs above 5σ in the FULL/LORES map. We also show the counts using seven SMGs that do not have $z_{\text{spec}} = 3.09$. Previous ALMA results (Karim et al. 2013; Ono et al. 2014; Simpson et al. 2015a; Fujimoto et al. 2016; Hatsukade et al. 2016; Oteo et al. 2016) are also shown. The flux density of the counts are scaled to 1.1 mm flux density, assuming a modified black body (similar with Figure 9; $S_{1.1\text{mm}}/S_{870\mu\text{m}} = 0.56$, $S_{1.1\text{mm}}/S_{1.2\text{mm}} = 1.29$, $S_{1.1\text{mm}}/S_{1.3\text{mm}} = 1.48$). The gray curve is the best-fit functions of a double-power law for the counts from our seven SMGs without $z = 3.09$, Karim et al. (2013), and Simpson et al. (2015a). The cumulative counts from 17 SMGs shows about five times excess at $S_{1.1\text{mm}} \gtrsim 1.0$ mJy, which should be caused by the $z = 3.09$ protocluster.

located outside of the AzTEC beam. Therefore, our results show that the ALMA mosaic is capable of finding such bright SMGs that were missed by previous submm/mm surveys taken with single-dish telescopes.

4.1.2. The Origin of Multiplicity in a Overdense Environment

There has been a debate on whether multiple individual SMGs of sources that are identified with a single-dish telescope are physically connected or instead are just a line-of sight projection (e.g., Ivison et al. 2007; Wang et al. 2011; Hayward et al. 2013; Hodge et al. 2013a; Cowley et al. 2015; Simpson et al. 2015a). For one source, Wang et al. (2011) proposed that it was composed of multiple, physically unrelated SMGs. In contrast, Tadaki et al. (2015) showed that one AzTEC source fragments into two H α emitters at $z = 2.53$, which supports the physical connection between the two (see also Yamaguchi et al. 2016). Simpson et al. (2015a) suggested that a portion of bright submm sources arise from physically related SMGs because the number of detected ALMA SMGs in the vicinity of the SCUBA2 sources are two orders of magnitude higher than the general field. On the other hand, recently Cowley et al. (2015) claimed that physically unrelated SMGs can also reproduce the single-dish sources in their semi-analytic model (see also Hayward et al. 2013).

Among 18 SMGs in ADF22, 11 SMGs have z_{spec} (Umehata et al. 2015; in preparation), 10 of which are at $z = 3.085\text{--}3.097$ (Table 2). All of the brightest ALMA counterparts of the AzTEC sources are at $z = 3.09$ and AzTEC1 and AzTEC14 have multiple ALMA SMGs at $z \simeq 3.09$ within the AzTEC beam ($d \sim 230$ kpc at $z = 3$). These results favor the hypothesis that physically connected multiple SMGs appear as a single single-dish source, at least in dense environments such as the center of a protocluster. The overdensity of galaxies

on such scales is conducive to mergers and dissipative interactions (e.g., Trainor & Steidel 2012) and hence such small-scale over-densities of SMGs may indicate that SMGs undergo merger-induced star formation. Furthermore, there are other $z = 3.09$ ALMA SMGs outside the AzTEC beam across the entire field of ADF22 (Figure 7, Table 2). This suggests that intense dusty star formation may also be enhanced by the environment on a large-scale (Umehata et al. 2015; see also Blain et al. 2004; Tamura et al. 2009; Umehata et al. 2014; Casey et al. 2015; Casey 2016; Hung et al. 2016).

4.2. Size Measurement and Star Formation Rate Surface Density

Two-dimensional Gaussian fits to the ALMA SMGs in the image plane, using the DEEP/HIRES map, suggest that ADF22 sources are generally resolved. The results for the nine brightest SMGs with S/N > 10 are summarized in Table 3. The deconvolved major axes are $0''.25\text{--}0''.85$, and the median value for the nine SMGs is $0''.32^{+0''.13}_{-0''.06}$ (Gaussian FWHM; $2.4^{+1.0}_{-0.4}$ physical kpc at $z = 3.09$). Seven of the nine SMGs have $z_{\text{spec}} \simeq 3.09$, which leads the almost same median value, $0''.32^{+0''.13}_{-0''.07}$ if we only consider such robust protocluster members. The size distribution in ADF22 is generally consistent with previous measurements for SMGs in other fields (Figure 9). Simpson et al. (2015b) measured the size for 23 bright SMGs observed at $870 \mu\text{m}$ and derived a median angular size FWHM = $0''.30 \pm 0''.04$. Ikarashi et al. (2015) reported that 13 SMGs, which were observed at 1.1 mm and thought to be at $z \sim 3\text{--}6$, have a median FWHM of $0''.20^{+0''.03}_{-0''.05}$. These results suggest that dusty star formation occurs in compact regions, a few kiloparsecs in extent. There does not appear to be a significant difference between the size of SMGs within the $z = 3.09$ protocluster and other SMGs. This might

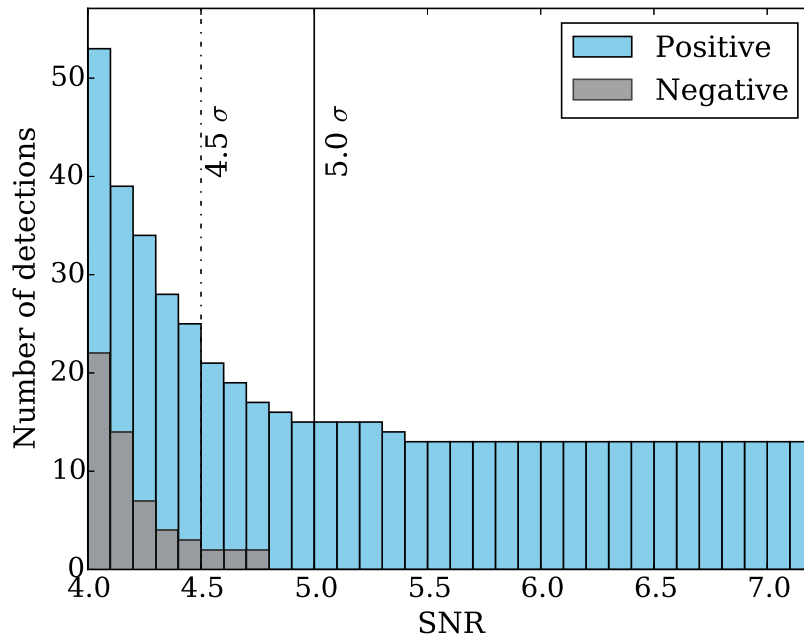


Figure 11. Cumulative number of positive and negative peaks in the DEEP/HIRES map. There are no negative peaks above 5σ . We adopt 4.5σ as a tentative detection limit for the DEEP/HIRES map. Above this limit, there is one negative peak.

Table 4
Differential and Cumulative Number Counts for all SMGs

Differential Counts					Cumulative Counts				
$S_{1.1\text{mm}}$ (mJy)	N_{all}	dN/dS ($10^3 \text{ mJy}^{-1} \text{ deg}^{-2}$)	N_{field}	dN/dS ($10^3 \text{ mJy}^{-1} \text{ deg}^{-2}$)	$S_{1.1\text{mm}}$ (mJy)	N_{all}	$N(>S)$ (10^3 deg^{-2})	N_{field}	$N(>S)$ (10^3 deg^{-2})
0.64	9	$9.4^{+6.1}_{-2.6}$	5	$5.6^{+4.6}_{-1.9}$	0.40	17	$9.8^{+5.1}_{-2.2}$	7	$4.4^{+3.3}_{-1.3}$
1.59	7	$2.4^{+2.1}_{-0.8}$	2	$0.7^{+1.1}_{-0.4}$	1.00	8	$4.1^{+3.4}_{-1.4}$	2	$1.0^{+1.7}_{-0.6}$
4.00	1	$0.1^{+0.3}_{-0.1}$	0	...	2.52	1	$0.5^{+1.2}_{-0.4}$	0	...

Note. We calculated the differential and cumulative counts in two ways: using all 17 SMGs (all) or the seven SMGs without $z_{\text{spec}} = 3.09$ (*field*). The errors are 1σ Poisson errors (Gehrels 1986).

suggest that the local mechanism triggering intense starbursts does not significantly depend on the large-scale environment.

The radio continuum also provides a tool to measure the scales of dusty starburst galaxies like SMGs (e.g., Chapman et al. 2004b; Biggs & Ivison 2008; Rujopakarn et al. 2016). These measurements show relatively extended profiles (e.g., a median of 5 kpc; Biggs & Ivison 2008), which is larger than the bright ALMA SMGs discussed above. To date, multiple explanations have been proposed. For instance, Rujopakarn et al. (2016) suggest that the relatively compact star formation is seen in SMGs with higher star formation rate (SFR), whereas main-sequence star-forming galaxies have different scales. Simpson et al. (2015b) indicate that the difference between the diffusion length of cosmic rays and FIR photons can account for it. In the future, deep and high angular resolution radio imaging in ADF22 should provide us with important clues to clarify the origin of the discrepancy between the radio and FIR sizes of SMGs.

The flux density and measured source size allow us to derive star formation rate surface density (Σ_{SFR}) and investigate the condition of star formation. We estimated L_{IR} [8–1000 μm] using SED templates of well-studied starburst galaxies (Silva

et al. 1998; Swinbank et al. 2010, 2014) in the same manner as in Umehata et al. (2015). The SFR is in turn derived from L_{IR} , using the empirical calibration by Kennicutt (1998) adjusted to the Kroupa initial mass function (Kroupa 2001). Because ADF22.2 and ADF22.5 do not have z_{spec} , we assume $z = 3.0$ (a median value for AzTEC sources; Smolčić et al. 2012b). Finally, Σ_{SFR} was calculated using the size of the 1.1 mm continuum emission and the SFR divided by a factor of two, following Simpson et al. (2015b) (Table 3). The median value is $\Sigma_{\text{SFR}} = 50 M_{\odot} \text{ yr}^{-1} \text{ kpc}^{-2}$, significantly lower than the predicted Eddington limit for radiation pressure supported disks (e.g., Elmegreen 1999; Thompson et al. 2005; Younger et al. 2010; Andrews & Thompson 2011; Riechers et al. 2013, 2014). Therefore, starbursts seen in bright SMGs in ADF22 are not Eddington-limited as a whole. As some authors have noted (e.g., Simpson et al. 2015b), if SMGs have clumpy structure, the individual components might be Eddington-limited, as has been claimed from some recent high angular resolution ALMA images of the brightest SMGs (e.g., Hatsukade et al. 2015; Iono et al. 2016, but see also Hodge et al. 2016). Further observations capable of resolving sub-kpc structures ($\lesssim 0''.1$ angular resolution) are required to probe such a scenario for the SMGs in ADF22.

4.3. Number Counts

In this section, we report the 1.1 mm number counts in ADF22, which is one of the most fundamental parameters in describing the evolution of this population. Previously, there have been a number of studies investigating submm/mm number counts from a variety of ALMA data sets; LABOCA/SCUBA2 source follow-up (Karim et al. 2013; Simpson et al. 2015a), the use of a calibration field (Oteo et al. 2016), a wide range of archival data (Hatsukade et al. 2013; Ono et al. 2014; Carniani et al. 2015; Fujimoto et al. 2016), and contiguous mapping (Aravena et al. 2016; Dunlop et al. 2016; Hatsukade et al. 2016). Here, we present the number counts in a ~ 7 arcmin² contiguous field, in a remarkably high-density region of the early universe, well-suited for investigating the environmental dependence of SMG source counts.

To minimize contamination by false positives, we utilized only the 17 SMGs detected with $S/N > 5\sigma$ in the FULL/LORES map. We excluded ADF22.18 because the S/N of this source is < 5 in the FULL/LORES map. To investigate how the existence of the $z = 3.09$ protocluster affects the counts, we calculated the counts in two ways. First, we included all 17 SMGs. Second, we exclude the ten SMGs with known $z_{\text{spec}} = 3.09$ (Table 2) and used only the remaining seven SMGs. Flux-boosting effects were not considered (see Section 3.2). We corrected for the completeness of the source extraction, although the counts should not be significantly affected by the correction. We calculated the number counts and associated errors in the same way as Hatsukade et al. (2016). Figure 10 shows the differential and cumulative counts (in the left and right panels, respectively). We show the counts from all 17 SMGs, and those obtained when we remove the ten sources with $z_{\text{spec}} = 3.09$. We also summarize the count statistics in Table 4. For comparison, we also show other ALMA counts in both panels of Figure 10 (Karim et al. 2013; Ono et al. 2014; Simpson et al. 2015a; Fujimoto et al. 2016; Oteo et al. 2016) by scaling to 1.1 mm, assuming a modified black body with typical values for SMGs (spectral index of $\beta = 1.5$, dust temperature of 35 K (e.g., Swinbank et al. 2014) and $z = 2.5$ where necessary).

As discussed in Umehata et al. (2015), the volume density of the ALMA SMGs at $z = 3.09$ in ADF22 is, at least, about three orders of magnitude greater than the expected value in general fields. We now investigate whether the protocluster members affect the number counts or not, considering ALMA SMGs at all redshifts. As shown in Figure 10, we see a possible excess in both of the differential and cumulative counts (for all of 17 SMGs). In the case of cumulative counts, the counts in ADF22 are approximately five times higher than those found in ALESS at $S_{1.1\text{mm}} > 2$ mJy (Karim et al. 2013) and four to five times higher than those obtained at $S_{1.1\text{mm}} > 1$ mJy (Fujimoto et al. 2016; Oteo et al. 2016). The group of SMGs at $z = 3.09$ is undoubtedly responsible for this excess. On the other hand, we do not see an excess in the faintest bin (i.e., sub-mJy sources). A possible attribution is that the elevation of dusty star-forming activity in dense environment is significant only for relatively bright SMGs ($S_{1.1\text{mm}} \gtrsim 1$ mJy). Deeper observation in the future will provide an answer.

Here, another question naturally arises. What are the counts in typical fields? The core of the SSA22 protocluster is an unusual environment. Therefore, we have to identify ALMA SMGs that are not associated with the protocluster and utilize

them in calculating the source counts in a typical field. It is, however, difficult to derive the counts correctly because seven sources with $\geq 5\sigma$ do not yet have z_{spec} . Here, we conservatively created counts using all seven ALMA SMGs (see Figure 10), some of which may also be at $z = 3.09$. The cumulative source counts from the seven SMGs and previous counts at bright fluxes (Karim et al. 2013; Simpson et al. 2015a) are fitted to a double-power law function of the form, $N(>S) = N'/S'[(S/S')^\alpha + (S/S')^\beta]^{-1}$, which yields the best-fit parameters of $N' = 200 \pm 30 \text{ deg}^{-2}$, $S' = 4.9 \pm 0.2$ mJy, $\alpha = 10.4 \pm 1.6$, and $\beta = 1.9 \pm 0.1$ (the right panel of Figure 10). Our counts, excluding known protocluster members, are in reasonable agreement with recent estimates that ought to be relatively free of cosmic variance; those from a number of calibration fields (Oteo et al. 2016) and those from a 2 arcmin² contiguous survey (Hatsukade et al. 2016). On the one hand, those counts from the seven SMGs seem to be several times lower than Fujimoto et al. (2016) at $S_{1.1\text{mm}} < 1$ mJy. One possible explanation for this discrepancy is that previous counts using $3\text{--}4\sigma$ sources are seriously affected by contaminants, as pointed out by Oteo et al. (2016). Another explanation involves clustering, although this effect may also contribute to our counts. The counts derived from serendipitously detected sources around other targeted galaxies might be biased or clustered as mentioned in previous papers (e.g., Simpson et al. 2015a; Fujimoto et al. 2016).

Our results suggest that the cluster environments are recognizable in the SMG number counts. At the same time, there are still large uncertainties for submm/mm number counts, including field to field variation, the shape of dust SEDs, and absolute flux uncertainties. Forthcoming, much wider ALMA surveys with sufficient depth, covering a variety of environments, should significantly improve our understanding of the submm/mm counts and their dependence on environment.

5. SUMMARY

We have presented the results from a 103-pointing ALMA 1.1 mm mosaic in the SSA22 field. We covered a 7 arcmin² area contiguously at the junction of a 50 Mpc scale cosmic large-scale structure at $z = 3.09$ containing three 1.1 mm sources discovered previously by the AzTEC/ASTE survey. Observations were conducted in 2014 and 2015 with different array configurations; therefore, we created two maps to handle the different angular resolution data; a $1''$ —tapered map (FULL/LORES map), and a $0''.7$ resolution map (DEEP/HIRES map). These maps reach a median rms noise of $75 \mu\text{Jy beam}^{-1}$ and $60 \mu\text{Jy beam}^{-1}$, respectively. Applying our source-detection algorithm to our two maps, we discover 18 robust ALMA SMGs with $S/N > 5$, with 1.1 mm flux density $S_{1.1\text{mm}} = 0.44\text{--}5.60$ mJy beam⁻¹, corresponding to $L_{\text{IR}} \simeq 8 \times 10^{11}\text{--}1 \times 10^{13} L_{\odot}$ at $z = 3$.

Through a comparison between the AzTEC map and the ALMA map of ADF22, we have found that three single-dish (AzTEC) sources are resolved into eight discrete ALMA SMGs. This suggests that multiple dusty galaxies may often contribute to one bright submm/mm source discovered by single-dishes in dense protocluster environments. The flux densities of AzTEC sources are consistent with the sum of the flux densities of ALMA SMGs, within errors for two sources, AzTEC14 and AzTEC77, but not for a third (AzTEC1), possibly indicating that there are additional missing faint

Table 5
Properties of Tentative ADF22 Sources

(1) ALMA ID	(2) ALMA NAME	(3) σ_{ALMA} ($\mu\text{Jy beam}^{-1}$)	(4) $S_{\text{ALMA}}^{\text{pk}}$	(5) S_{ALMA} (mJy)	(6) Map
ADF22.19	ALMAJ221733.87+001646.1	63	4.3	0.29 ± 0.06	FULL/LORES
ADF22.20	ALMAJ221734.69+001635.2	68	4.3	0.67 ± 0.09	FULL/LORES
ADF22.21 ^a	ALMAJ221733.09+001718.5	78	4.3	0.79 ± 0.08	FULL/LORES
ADF22.22	ALMAJ221732.96+001636.0	67	4.3	0.42 ± 0.07	FULL/LORES
ADF22.23	ALMAJ221735.47+001805.1	65	4.2	0.30 ± 0.06	FULL/LORES
ADF22.24	ALMAJ221737.43+001723.0	67	4.1	0.56 ± 0.08	FULL/LORES
ADF22.25	ALMAJ221733.81+001656.5	72	4.1	0.44 ± 0.08	FULL/LORES
ADF22.26	ALMAJ221733.19+001752.7	82	4.1	0.63 ± 0.07	FULL/LORES
ADF22.27	ALMAJ221737.18+001832.0	85	4.0	0.25 ± 0.06	FULL/LORES
ADF22.28	ALMAJ221732.50+001729.5	78	4.0	0.48 ± 0.08	FULL/LORES
ADF22.29	ALMAJ221738.35+001710.8	109	4.0	1.12 ± 0.11	FULL/LORES
ADF22.30	ALMAJ221732.19+001642.0	63	4.7	0.29 ± 0.09	DEEP/HIRES
ADF22.31	ALMAJ221734.97+001527.6	64	4.6	0.41 ± 0.12	DEEP/HIRES
ADF22.32	ALMAJ221734.08+001632.6	59	4.5	0.35 ± 0.12	DEEP/HIRES

Note. Columns are generally similar with Table 2. We select 11 sources with $S/N \geq 4.0$ using the FULL/LORES map. We also include three sources with $S/N \geq 4.5$ (but not selected using the FULL/LORES map) on the basis of the DEEP/HIRES map. In total, 14 tentative sources are found.

^a CO(4-3) line at $z = 0.71$ is detected and identified using the band 6 cube (N. Hayatsu et al. 2016, in preparation).

and/or diffuse dusty galaxies remaining undetected in the ALMA map. Ten out of 18 SMGs in our sample are known to lie at $z = 3.09$. The fact that multiple $z = 3.09$ ALMA SMGs are found to comprise two of three of the single-dish (AzTEC) sources suggests that, at least in dense protocluster environments, interactions may be responsible for a significant fraction of observed SMG multiplicity.

The ALMA SMGs are generally resolved in our data. We measured the deconvolved source size for the nine brightest ALMA SMGs with $>10\sigma$, conducting Gaussian fitting to the ALMA SMGs. The median size of $0''.32_{-0.06}^{+0.13}$ ($2.4_{-0.4}^{+1.0}$ physical kpc at $z = 3.09$) agrees well with previous measurements, and there is no recognizable difference between the size of $z = 3.09$ protocluster members and the ALMA SMGs in other fields.

We derived the 1.1 mm source counts using all 17 SMGs above 5σ from the FULL/LORES map, as well as the seven SMGs without $z_{\text{spec}} = 3.09$. The counts of 17 SMGs are about five times higher than the counts in typical fields at $S_{1.1\text{mm}} \gtrsim 1$ mJy, which is caused by the $z = 3.09$ SMG concentration associated with the protocluster. On the other hand, we found that the source counts in ADF22 are consistent with recent unbiased ALMA counts when we exclude known members of the $z = 3.09$ structure.

In conclusion, we have obtained deep and high angular resolution imaging covering a certain area using ALMA, which demonstrated that there is an unusual number of dusty galaxies residing at the core of the $z = 3.09$ protocluster. This observation provides a basis for understanding the formation of dusty galaxies within cosmic large-scale structure in the early universe.

We deeply appreciate the anonymous referee for a significant number of valuable comments. We are thankful for Ken Mawatari for helping us to compile redshift catalogs of $z = 3.09$ LAEs and LBGs in the literature. H.U. is supported by the ALMA Japan Research Grant of NAOJ Chile Observatory, NAOJ-ALMA-0071, 0131, 140, and 0152. H.U. is also supported by JSPS Grant-in-Aid for Research Activity

Start-up (16H06713). Y.T. is supported by JSPS KAKENHI No. 15H02073. R.J.I. acknowledges support from ERC in the form of the Advanced Investigator Programme, 321302, COSMICISM. I.R.S. and D.M.A. acknowledge support from STFC (ST/L00075X/1). I.R.S. acknowledges support from the ERC Advanced Investigator program DUSTYGAL 321334, and a Royal Society/Wolfson Merit Award. S.I. acknowledges the support of the Netherlands Organization for Scientific Research (NWO) through the Top Grant Project 614.001.403. This paper makes use of the following ALMA data: ADS/JAO.ALMA#2013.1.00162.S. ALMA is a partnership of ESO (representing its member states), NSF (USA), and NINS (Japan), along with NRC (Canada), NSC and ASIAA (Taiwan), and KASI (Republic of Korea), in cooperation with the Republic of Chile. The Joint ALMA Observatory is operated by ESO, AUI/NRAO, and NAOJ.

Facility: ALMA.

APPENDIX A TENTATIVE SOURCE CATALOG

In addition to the robust samples of 18 ALMA SMGs with $>5\sigma$ detection, there are also some possible source candidates with slightly lower significances (Table 5). Considering the result from our test using negative maps shown in Figures 4 and 11, we adopt 4.0σ and 4.5σ as tentative detection thresholds for the FULL/LORES and DEEP/HIRES maps, respectively. The test suggests that about half of these sources detected tentatively may be false detections, and therefore we need to be careful in utilizing the catalog.

APPENDIX B CATALOGS OF PROTO-CLUSTER MEMBERS IN ADF22

Previously known galaxies selected at varying wavelengths and located in ADF22 are summarized in Table 6.

Table 6
Known Member Galaxies of the $z = 3.09$ Proto-cluster in ADF22

(1) Galaxy	(2) Coordinate (J2000)	(3) z_{spec}	(4) Type	(5) IDs	(6) ALMA source
LAEs					
001	22:17:33.10 +00:18:29.0	3.090	Ly α	(M05)	...
002	22:17:35.61 +00:18:00.2	3.091	Ly α	016 (N13)	...
003	22:17:31.73 +00:16:06.9	3.101	Ly α	023 (N13)	...
004	22:17:34.17 +00:16:09.7	3.096	Ly α	024 (N13)	...
005	22:17:36.74 +00:16:28.8	3.091	Ly α	025 (N13)	...
006	22:17:31.80 +00:17:17.9	3.088	Ly α	028 (N13)	...
007	22:17:33.63 +00:17:15.1	3.092	Ly α	031 (N13)	...
008	22:17:34.77 +00:15:41.3	3.099	Ly α	038 (N13)	...
009	22:17:35.97 +00:16:30.2	3.094	Ly α	045 (N13)	...
010	22:17:34.70 +00:16:33.4	3.090	Ly α	053 (N13)	...
011	22:17:34.10 +00:15:40.2	3.101	Ly α	061 (N13)	...
012	22:17:31.24 +00:17:32.1	3.084	Ly α	072 (N13)	...
		3.0845	[O III] λ 5007	072 (E14)	...
013	22:17:37.68 +00:16:48.3	3.090	Ly α	078 (N13)	...
		3.0870	[O III] λ 5007	078 (E14)	...
014	22:17:35.44 +00:16:47.6	3.087	Ly α	082 (N13)	...
		3.0873	[O III] λ 5007	082 (E14)	...
015	22:17:36.14 +00:15:40.7	3.095	Ly α	091 (N13)	...
016	22:17:31.14 +00:16:42.9	3.096	Ly α	111 (N13)	...
017	22:17:32.72 +00:15:54.2	3.096	Ly α	112 (N13)	...
018	22:17:33.46 +00:17:01.2	3.093	Ly α	115 (N13)	...
019	22:17:32.84 +00:16:48.8	3.092	Ly α	130 (N13)	...
LBGs					
001	22:17:31.49+00:16:31.2	3.098	Ly α	M25 (N13)	...
002	22:17:31.66+00:16:58.0	3.094	Ly α	M28, 012 (S03; N13)	...
		3.0902	[O III] λ 5007	012 (E14)	...
003	22:17:36.87+00:17:12.4	3.099	Ly α	M31 (N13)	...
004	22:17:33.80+00:17:57.2	3.084	Ly α	M34 (N13)	...
005	22:17:37.66+00:18:20.9	3.086	Ly α (abs)	C50 (S03)	...
K-band selected galaxies					
001	22:17:37.1+00:17:12.4	3.0899	[O III] λ 5007	(K15)	ADF22.8
002	22:17:37.3+00:16:30.7	3.0888	[O III] λ 5007	(K15)	...
003	22:17:36.5+00:16:22.6	3.0945	[O III] λ 5007	(K15)	ADF22.9
004	22:17:31.8+00:16:06.3	3.0981	[O III] λ 5007	(K15)	...
005	22:17:32.0+00:16:55.5	3.0909	[O III] λ 5007	(K15)	ADF22.12
006	22:17:37.3+00:18:23.2	3.0851	[O III] λ 5007	K15a (K15; K16)	...
007	22:17:36.8+00:18:18.2	3.0854	[O III] λ 5007	K15b (K15; K16)	ADF22.16
008	22:17:37.1+00:18:17.9	3.0774	[O III] λ 5007	K15d (K15; K16)	...
009	22:17:37.1+00:18:22.4	3.0925	[O III] λ 5007	K15e (K15; K16)	ADF22.11
010	22:17:36.9+00:18:38.0	3.0866	[O III] λ 5007	K15f (K15; K16)	...
X-ray sources and LABs					
001	22:17:32.0+00:16:55.6	3.091	[O III] λ 5007	114 (L09), LAB12 (M04; G09)	ADF22.12
002	22:17:32.2,+00:17:36.0	3.097	[CII] 158 μ m	116 (L09)	ADF22.7
003	22:17:32.4,+00:17:43.9	3.092	CO(3–2)	120 (L09)	ADF22.1
004	22:17:35.8,+00:15:59.1	3.089	Ly α	139 (L09), LAB14 (M04; G09)	ADF22.6
005	22:17:36.5,+00:16:22.6	3.084	Ly α	140 (L09), QSO (S98)	ADF22.9
006	22:17:37.0,+00:18:20.8	3.091	CO(9–8), [CII] 158 μ m	142 (L09)	ADF22.4
007	22:17:37.3,+00:16:30.7	3.0888	[O III] λ 5007	144 (L09)	...
008	22:17:37.3,+00:18:23.5	3.0851	[O III] λ 5007	145 (L09)	...

Note. (1) Galaxy population and IDs in this work. There are overlaps between K-band selected galaxies and X-ray sources/LABs. (2) Coordinates in the literatures. (3), (4) Spectroscopic redshifts and the line used to determine redshifts. (5) IDs in the literatures (Matsuda et al. (2005) (M05), Nestor et al. (2013) (N13), Erb et al. (2014) (E14), Steidel et al. (2003) (S03), Kubo et al. (2015) (K15), Kubo et al. (2016) (K16), Lehmer et al. (2009) (L09), Matsuda et al. (2004) (M04), Geach et al. (2009) (G09)). The redshift determination of X-ray sources and ALMA sources are described in Umehata et al. (2015) and this work. (6) IDs of ALMA counterparts in ADF22.

REFERENCES

- Alexander, D. M., Simpson, J. M., Harrison, C. M., et al. 2016, *MNRAS*, **461**, 2944
- Andrews, B. H., & Thompson, T. A. 2011, *ApJ*, **727**, 97
- Aravena, M., Decarli, R., Walter, F., et al. 2016, *ApJ*, **833**, 68
- Barger, A. J., Wang, W.-H., Cowie, L. L., et al. 2012, *ApJ*, **761**, 89
- Biggs, A. D., & Ivison, R. J. 2008, *MNRAS*, **385**, 893
- Blain, A. W., Chapman, S. C., Smail, I., & Ivison, R. 2004, *ApJ*, **611**, 725
- Blain, A. W., Smail, I., Ivison, R. J., Kneib, J.-P., & Frayer, D. T. 2002, *PhR*, **369**, 111
- Bothwell, M. S., Smail, I., Chapman, S. C., et al. 2013, *MNRAS*, **429**, 3047
- Capak, P. L., Riechers, D., Scoville, N. Z., et al. 2011, *Natur*, **470**, 233
- Carniani, S., Maiolino, R., De Zotti, G., et al. 2015, *A&A*, **584**, A78
- Casey, C. M. 2016, *ApJ*, **824**, 36
- Casey, C. M., Cooray, A., Capak, P., et al. 2015, *ApJL*, **808**, L33
- Casey, C. M., Narayanan, D., & Cooray, A. 2014, *PhR*, **541**, 45
- Chapman, S. C., Blain, A. W., Smail, I., & Ivison, R. J. 2005, *ApJ*, **622**, 772
- Chapman, S. C., Smail, I., Blain, A. W., & Ivison, R. J. 2004a, *ApJ*, **614**, 671
- Chapman, S. C., Smail, I., Windhorst, R., Muxlow, T., & Ivison, R. J. 2004b, *ApJ*, **611**, 732
- Clements, D. L., Braglia, F., Petitpas, G., et al. 2016, *MNRAS*, **461**, 1719
- Collins, C. A., Stott, J. P., Hilton, M., et al. 2009, *Natur*, **458**, 603
- Coppin, K., Chapin, E. L., Mortier, A. M. J., et al. 2006, *MNRAS*, **372**, 1621
- Cowley, W. I., Lacey, C. G., Baugh, C. M., & Cole, S. 2015, *MNRAS*, **446**, 1784
- Daddi, E., Dannerbauer, H., Stern, D., et al. 2009, *ApJ*, **694**, 1517
- Dannerbauer, H., Kurk, J. D., De Breuck, C., et al. 2014, *A&A*, **570**, A55
- De Lucia, G., Springel, V., White, S. D. M., Croton, D., & Kauffmann, G. 2006, *MNRAS*, **366**, 499
- Dressler, A. 1980, *ApJ*, **236**, 351
- Dunlop, J. S., McLure, R. J., Biggs, A. D., et al. 2016, arXiv:1606.00227
- Elmegreen, B. G. 1999, *ApJ*, **517**, 103
- Erb, D. K., Steidel, C. C., Trainor, R. F., et al. 2014, *ApJ*, **795**, 33
- Fujimoto, S., Ouchi, M., Ono, Y., et al. 2016, *ApJS*, **222**, 1
- Geach, J. E., Alexander, D. M., Lehmer, B. D., et al. 2009, *ApJ*, **700**, 1
- Geach, J. E., Bower, R. G., Alexander, D. M., et al. 2014, *ApJ*, **793**, 22
- Geach, J. E., Matsuda, Y., Smail, I., et al. 2005, *MNRAS*, **363**, 1398
- Gear, W. K., Lilly, S. J., Stevens, J. A., et al. 2000, *MNRAS*, **316**, L51
- Gehrels, N. 1986, *ApJ*, **303**, 336
- Gobat, R., Daddi, E., Onodera, M., et al. 2011, *A&A*, **526**, A133
- Greve, T. R., Bertoldi, F., Smail, I., et al. 2005, *MNRAS*, **359**, 1165
- Hancock, P. J., Murphy, T., Gaensler, B. M., Hopkins, A., & Curran, J. R. 2012, *MNRAS*, **422**, 1812
- Hatsukade, B., Kohno, K., Umehata, H., et al. 2016, *PASJ*, **68**, 36
- Hatsukade, B., Ohta, K., Seko, A., Yabe, K., & Akiyama, M. 2013, *ApJL*, **769**, L27
- Hatsukade, B., Tamura, Y., Iono, D., et al. 2015, *PASJ*, **67**, 93
- Hayashino, T., Matsuda, Y., Tamura, H., et al. 2004, *AJ*, **128**, 2073
- Hayward, C. C., Behroozi, P. S., Somerville, R. S., et al. 2013, *MNRAS*, **434**, 2572
- Hodge, J. A., Carilli, C. L., Walter, F., Daddi, E., & Riechers, D. 2013a, *ApJ*, **776**, 22
- Hodge, J. A., Karim, A., Smail, I., et al. 2013b, *ApJ*, **768**, 91
- Hodge, J. A., Swinbank, A. M., Simpson, J. M., et al. 2016, *ApJ*, **833**, 103
- Hogg, D. W., & Turner, E. L. 1998, *PASP*, **110**, 727
- Hung, C.-L., Casey, C. M., Chiang, Y.-K., et al. 2016, *ApJ*, **826**, 130
- Ikarashi, S., Ivison, R. J., Caputi, K. I., et al. 2015, *ApJ*, **810**, 133
- Iono, D., Yun, M. S., Aretxaga, I., et al. 2016, *ApJL*, **829**, L10
- Ivison, R. J., Greve, T. R., Dunlop, J. S., et al. 2007, *MNRAS*, **380**, 199
- Karim, A., Swinbank, A. M., Hodge, J. A., et al. 2013, *MNRAS*, **432**, 2
- Kato, Y., Matsuda, Y., Smail, I., et al. 2016, *MNRAS*, **460**, 3861
- Kennicutt, R. C., Jr. 1998, *ARA&A*, **36**, 189
- Kroupa, P. 2001, *MNRAS*, **322**, 231
- Kubo, M., Uchimoto, Y. K., Yamada, T., et al. 2013, *ApJ*, **778**, 170
- Kubo, M., Yamada, T., Ichikawa, T., et al. 2015, *ApJ*, **799**, 38
- Kubo, M., Yamada, T., Ichikawa, T., et al. 2016, *MNRAS*, **455**, 3333
- Lehmer, B. D., Alexander, D. M., Chapman, S. C., et al. 2009, *MNRAS*, **400**, 299
- Matsuda, Y., Yamada, T., Hayashino, T., et al. 2004, *AJ*, **128**, 569
- Matsuda, Y., Yamada, T., Hayashino, T., et al. 2005, *ApJL*, **634**, L125
- McMullin, J. P., Waters, B., Schiebel, D., Young, W., & Golap, K. 2007, in ASP Conf. Ser. 376, *Astronomical Data Analysis Software and Systems XVI*, ed. R. A. Shaw, F. Hill, & D. J. Bell (San Francisco, CA: ASP), 127
- Miettinen, O., Smolčić, V., Novak, M., et al. 2015, *A&A*, **577**, A29
- Nelan, J. E., Smith, R. J., Hudson, M. J., et al. 2005, *ApJ*, **632**, 137
- Nestor, D. B., Shapley, A. E., Kornei, K. A., Steidel, C. C., & Siana, B. 2013, *ApJ*, **765**, 47
- Ono, Y., Ouchi, M., Kurono, Y., & Momose, R. 2014, *ApJ*, **795**, 5
- Oteo, I., Zwaan, M. A., Ivison, R. J., Smail, I., & Biggs, A. D. 2016, *ApJ*, **822**, 36
- Planck Collaboration, Aghanim, N., Altieri, B., et al. 2015, *A&A*, **582**, A30
- Postman, M., & Geller, M. J. 1984, *ApJ*, **281**, 95
- Riechers, D. A., Bradford, C. M., Clements, D. L., et al. 2013, *Natur*, **496**, 329
- Riechers, D. A., Carilli, C. L., Capak, P. L., et al. 2014, *ApJ*, **796**, 84
- Rujopakarn, W., Dunlop, J. S., Rieke, G. H., et al. 2016, *ApJ*, **833**, 12
- Scott, S. E., Dunlop, J. S., & Serjeant, S. 2006, *MNRAS*, **370**, 1057
- Scott, S. E., Fox, M. J., Dunlop, J. S., et al. 2002, *MNRAS*, **331**, 817
- Silva, L., Granato, G. L., Bressan, A., & Danese, L. 1998, *ApJ*, **509**, 103
- Simpson, J. M., Smail, I., Swinbank, A. M., et al. 2015a, *ApJ*, **807**, 128
- Simpson, J. M., Smail, I., Swinbank, A. M., et al. 2015b, *ApJ*, **799**, 81
- Simpson, J. M., Swinbank, A. M., Smail, I., et al. 2014, *ApJ*, **788**, 125
- Smolčić, V., Aravena, M., Navarrete, F., et al. 2012a, *A&A*, **548**, A4
- Smolčić, V., Navarrete, F., Aravena, M., et al. 2012b, *ApJS*, **200**, 10
- Steidel, C. C., Adelberger, K. L., Dickinson, M., et al. 1998, *ApJ*, **492**, 428
- Steidel, C. C., Adelberger, K. L., Shapley, A. E., et al. 2000, *ApJ*, **532**, 170
- Steidel, C. C., Adelberger, K. L., Shapley, A. E., et al. 2003, *ApJ*, **592**, 728
- Swinbank, A. M., Simpson, J. M., Smail, I., et al. 2014, *MNRAS*, **438**, 1267
- Swinbank, A. M., Smail, I., Longmore, S., et al. 2010, *Natur*, **464**, 733
- Tacconi, L. J., Neri, R., Chapman, S. C., et al. 2006, *ApJ*, **640**, 228
- Tadaki, K.-i., Kohno, K., Kodama, T., et al. 2015, *ApJL*, **811**, L3
- Tamura, Y., Iono, D., Wilner, D. J., et al. 2010, *ApJ*, **724**, 1270
- Tamura, Y., Kohno, K., Nakanishi, K., et al. 2009, *Natur*, **459**, 61
- Thompson, T. A., Quataert, E., & Murray, N. 2005, *ApJ*, **630**, 167
- Trainor, R. F., & Steidel, C. C. 2012, *ApJ*, **752**, 39
- Uchimoto, Y. K., Yamada, T., Kajisawa, M., et al. 2012, *ApJ*, **750**, 116
- Umehata, H., Tamura, Y., Kohno, K., et al. 2014, *MNRAS*, **440**, 3462
- Umehata, H., Tamura, Y., Kohno, K., et al. 2015, *ApJL*, **815**, L8
- Walter, F., Decarli, R., Aravena, M., et al. 2016, arXiv:1607.06768
- Wang, W.-H., Cowie, L. L., Barger, A. J., & Williams, J. P. 2011, *ApJL*, **726**, L18
- Yamada, T., Nakamura, Y., Matsuda, Y., et al. 2012, *AJ*, **143**, 79
- Yamaguchi, Y., Tamura, Y., Kohno, K., et al. 2016, *PASJ*, **68**, 82
- Younger, J. D., Dunlop, J. S., Peck, A. B., et al. 2008, *MNRAS*, **387**, 707
- Younger, J. D., Fazio, G. G., Ashby, M. L. N., et al. 2010, *MNRAS*, **407**, 1268